

Panetta, Paul. (2018). Quantitative Measurement of In-Situ Burn (ISB) Efficiency and Rate. (Bureau of Safety and Environmental Enforcement Oil Spill Response Research Project # 1074).

Bureau of Safety and Environmental Enforcement (BSEE) Report: Quantitative Measurement of In-Situ Burn (ISB) Efficiency and Rate

Paul D. Panetta, Richard Byrne, and Hualong Du



Final Report

Quantitative Measurement of In-Situ Burn (ISB)
Efficiency and Rate

Paul D. Panetta, Richard Byrne, and Hualong Du

Applied Research Associates, Inc.

Report for

U.S. Department of the Interior
Bureau of Safety and Environmental Enforcement (BSEE)
Sterling, VA

September 2018



This study was funded by the Bureau of Safety and Environmental Enforcement (BSEE), U.S. Department of the Interior, Washington, D.C., under Contract Number E15PC00005.

Acknowledgments

The authors wish to thank Leonard Zabilansky and Nate Lamie from the Cold Regions Research and Engineering Laboratory (CRREL), Ali Rangwala, Kemal Arsava and the team at the Worcester Polytechnic Institute (WPI), Kevin Panetta from ARA for assistance with ISB at the Virginia Institute of Marine Science (VIMS) and in designing the measurement apparatus for lab measurements of the speed of sound of hot oil and L. N. Ferris from VIMS for assisting with the ISB measurements at VIMS and converting the videos of the scale measurements to numerical readouts, and Professor Donglai Gong from VIMS for the aerial views of our burning from his drone mounted camera. We especially would like to thanks the Dr. Bill Lehr, Dr. Oscar Garcia-Pineda, Mr. Neré Mabile, and Dr. Tom Weber who carefully read the original report and provided valuable insight and ideas on how to improve both the report and this work.

Disclaimer

This final report has been reviewed by the BSEE and approved for publication. Approval does not signify that the contents necessarily reflect the views and policies of the BSEE, nor does mention of the trade names or commercial products constitute endorsement or recommendation for use.

Table of Contents

<i>Acknowledgments</i>	4
<i>Disclaimer</i>	4
<i>Executive Summary</i>	6
1. Overview and Objective	9
2. Method for determining the volume of burning oil	11
2.1. Surface Area of Burn	12
2.1.1. Area Computation	14
2.2. Thickness measurements using acoustics	18
2.2.1. Speed of sound in crude oil as a function of temperature	20
2.2.2. Temperature inside a burning oil slick	22
2.2.3. Thickness measurements in a burning oil slick	24
2.2.4. Validation of thickness measurement	27
3. Accuracy and precision of thickness measurements	28
4. Accuracy and precision of area estimate	32
4.1. Multiple Camera Error	37
4.2. Strategy For Area Computation	38
5. Burn rate and efficiency	39
6. Applications to various ISB scenarios	41
6.1. Contained burns at the outdoor ARA-VIMS burn facility	41
6.2. Contained burns at the indoor WPI Burn Lab	45
6.2.1. Area calculations of small contained burns	51
6.3. ISB of oil in small cavities of ice	53
6.3.1. Area measurement of ISB in ice fields	56
6.3.2. Acoustic measurement of thickness for ISB of ANS oil in ice fields	64
7. Transitioning Towards Operational Environments	72
7.1. Surface area measurements	72
7.2. Thickness measurements from free swimming ROV platform	72
8. Summary and Conclusions	74
9. Recommendations	75
10. References	77

Executive Summary

In-situ burning (ISB) is an important tool for removing oil from the environment during an oil spill. For an accurate oil budget calculation, it is critical to measure the amount of oil removed during ISB. The volume of oil consumed during ISB is typically computed using a manual, coarse, time integration of the instantaneous burning area based on visual observations assuming a burn rate. ISB is a dynamic process, the burning oil does not always fill the boomed area completely, and the burn rate depends on many factors including type of oil, degree of emulsification and weathering, estimated thickness, weather conditions, and size of the burn area. An accurate measure of the amount of oil removed is an important parameter for oil spill responders, regulators, those monitoring the environmental impact of the spill, and the organization responsible for spilling the oil.

While the method to determine the volume of burned oil is well codified, it does not incorporate any measurement of the thickness of the oil slick or a measurement of the degree of weathering of the oil. In addition, the efficiency of ISB can only be determined in the field if the amount of oil spilled is known and the residue collected. These inadequacies directly affect the accuracy and precision in determining burn rate, the efficiency, and thus the amount of oil removed and left in the environment. This manual process is extremely labor intensive, subjective, time consuming, and lacks the accuracy and precision that could be achieved if automated measurements of surface area and thickness existed.

To alleviate these inadequacies, we created the capability to measure the instantaneous burn rate and efficiency during ISB to provide a more accurate input into the oil budget and to provide actionable information during ISB operations. The capability is based on surface area measurements using both visible and infrared (IR) cameras at various locations around the burning oil and thickness measurements of the slick using acoustic sensors placed in the water under the burning oil. The volume measurements of the oil were benchmarked by weighing the oil during ISB by placing the entire apparatus on a scale and recording the weight lost during the burn. Our measurements yielded burn rates in the range of 0.2 mm/minute to over 7 mm/minute and efficiencies between 58% and 96% for Alaska North Slope (ANS) crude oil under various conditions including small contained burns inside and burn in ice fields. The capability developed by this work provides an unprecedented detailed ability to study the dynamics of ISB during burning with sub second time resolution.

We applied these measurements to ISB of various crude oils at our laboratory, at the burn laboratory at Worcester Polytechnic Institute, and in simulated ice fields at the Cold Regions Research and Engineering Laboratory (CRREL). We also directly measured the effects of the applications of herders on the thickness and burn rate of oil for applications towards the end of burning which will be reported in other publications. The acoustic thickness measurements were corrected for the high temperature gradient in the oil and combined with multi-camera automated burn area estimates to yield an accurate volume of oil consumed while burning. Using these methods one can identify the buildup of the burn, the active burning phase, and, in the case of confined burns, the vigorous burning phase where the underlying water boils and evaporates. During applications of herders,

we were able to measure the thickness increase and surface area contraction and, thus, the additional combusted oil. The measurements were applied to burning ANS, Rock, Agbami, diesel, and hexane. We also deployed the acoustic measurements of thickness from a remotely operated vehicle (ROV) platform at CRREL to begin the transition to open-water environments.

During this work, we advanced this technology through a large range of Technology Readiness Levels (TRLs). Specifically, at the start of this project the ability to directly measure the volume of burning did not exist. Acoustic measurements of slick thickness had only been used to measure the thickness of non-burning slicks from platforms that rolled along the bottom of the Ohmsett tank and only the image processing had been attempted on burning oil. At that stage, the technology was at TRL 2. By the end of the project, we advanced the technology through TRL 5 by performing the integrated measurements in the relevant environment at CRREL and started working on TRL 6 by deploying the acoustic measurements from a free-swimming ROV platform and image capture from a flying drone platform.

Continued advancement of the ISB measurement capability developed in this project should involve three parallel paths. One is to develop a deployable system to measure open water burns. The second is to develop a laboratory measurement apparatus and procedure for determining burn rates and efficiencies of oils. The third path is to determine the effects of oil chemical properties on burn rate and efficiency. Additionally, it would be useful to use our system to measure the potential improvement of efficiency that could be achieved by the application of herders at various times during burning.

For the field deployable system it will be important to measure the burn area and thickness and archive the results and the supporting imagery to a database for support in post analysis and determination of the volume of oil removed from the environment. The system should allow traversing the burn area with an ROV mounted thickness probe to map the wider oil distribution for accurate volume measurements as well as to guide where to place the boom and boat speeds to optimize the burn rate and efficiency.

Creating a laboratory system for ISB rate and efficiency using the capability developed in this work will be useful for the community because it will provide a turnkey system for determining the burn rates and efficiency of various oils as a function of emulsification, evaporation and photo-oxidation. The scale and shape of the apparatus, the use of water circulation to simulate open water convection, and the amount of oil used to start the burn are all significant in determining burn rates and efficiencies that are transferable to open water burning.

The effects of chemical properties of the oil on the burn rate and efficiency can also be closely studied using the capability developed. It would be important to measure the chemical properties of the oil during the burning by collecting samples throughout the burning process for offline chemical analysis such as the percentage of the sulfur, asphaltenes, resins, and aromatics (SARA) components, density, and spectral analysis. These studies would allow one to determine when each components burns off and how

they affect the burn rate and efficiency. In principle, one could perform the chemical analysis on unburned oil and predict the burn rate and efficiency.

1. Overview and Objective

In-situ burning (ISB) is an important tool to remove oil from the environment during an oil spill. For an accurate oil budget calculation, it is critical to quantify the amount of oil removed during ISB. The volume of oil consumed during ISB is typically computed using a manual, coarse, time integration of the instantaneous burning area based on visual observations assuming a burn rate for the particular oil and environment. ISB is a dynamic process, the burning oil does not always fill the boomed area completely, and the burn rate depends on many factors including type of oil, degree of emulsification, and weathering, estimated thickness, weather conditions, and size of the burn area. Figure 1 shows several ISB scenarios showing the incomplete filling of the boom. An accurate measure of the amount of oil removed is an important parameter for oil spill responders, regulators, those monitoring the environmental impact of the spill, and the organization responsible for spilling the oil.

The area of burning oil in the boom is estimated using a nomogram like the ones shown in Figure 2. The volume of oil burned is then estimated from the duration of a burn and literature values of the burn rate for that particular class of oil [1,2]. While well codified, this method relies on visual estimates of the area and tabular values of burn rate; however, it does not incorporate any measurement of the thickness of the oil slick. In addition, the efficiency of the ISB can only be determined in the field if the amount of oil spilled is known and the residue collected, which is impractical in a real spill. These inadequacies directly affect the accuracy and precision in determining burn rate, the efficiency, and, thus, the amount of oil removed and the amount remaining in the environment. This manual process is extremely labor intensive, subjective, time consuming, and lacks the accuracy and precision that could be achieved with the automated measurements of surface area and thickness we created during this work.



Figure 1. Images of ISB in open offshore water.

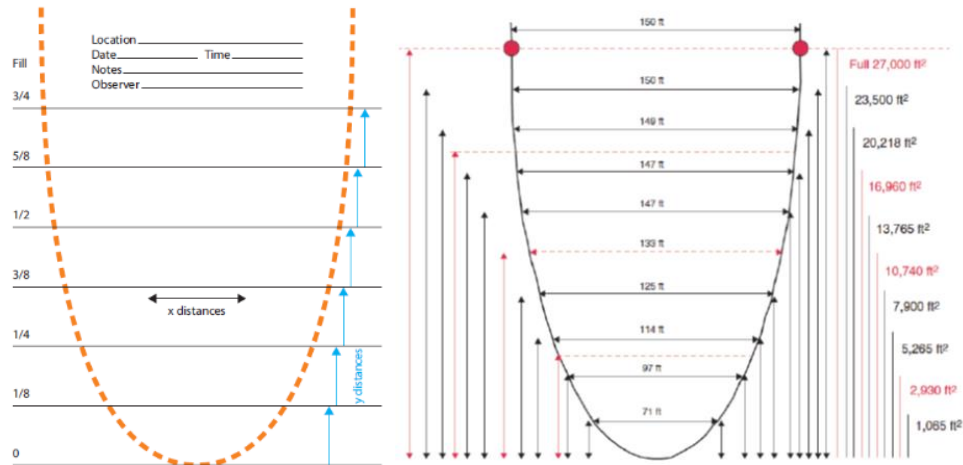


Figure 2. Nomogram used to record and visually estimate burn areas for a catenary shaped boom (left) [1] and with dimensions of the boom annotated on the nomogram (right) [2].

To alleviate these inadequacies, we created the capability to measure the instantaneous burn rate and efficiency during ISB to provide a more accurate input into the oil budget and to provide actionable information during ISB operations. The capability is based on surface area measurements using both visible and infrared (IR) cameras at various locations around the burning oil and thickness measurements of the slick using acoustic sensors placed in the water under the burning oil. The volume measurements of the oil, burn rate, and efficiency were benchmarked by weighing the oil during ISB by placing the entire apparatus on a scale and recording the weight during the burn. We also deployed the acoustic measurements of thickness from a ROV platform to begin the transition to open water environments.

We applied these measurements to ISB of various crude oils at our laboratory, at the burn laboratory at Worcester Polytechnic Institute (WPI), and in simulated ice fields at the Cold Regions Research and Engineering Laboratory (CRREL). The acoustic thickness measurements were corrected for the high temperature gradient in the oil combined with multi camera automated burn area estimates yielded an accurate volume of oil consumed while burning. We are able to identify the buildup of the burn, the active burning phase, and, in the case of confined burns, the vigorous burning phase. The measurements have been applied to burning ANS, Rock, Agbami, diesel, and hexane.

During this work, we advanced this technology through a tremendous number of Technology Readiness Levels (TRLs). Specifically, at the start of this project the ability to directly measure the volume of burning did not exist. Acoustic measurements of slick thickness had only been used to measure the thickness of non-burning slicks from static platforms or ones that rolled along the bottom of the Ohmsett tank and only the image processing had been attempted on burning oil. At that stage, the technology was at TRL 2. By the end of the project, we advanced the technology through TRL 5 by performing the integrated measurements in the relevant environment at CRREL and started working on TRL 6 by deploying the acoustic measurements from a free-swimming ROV platform and image capture from a flying drone platform.

In the remainder of the report, we will first describe the method for measuring the oil volume during ISB including the area and thickness measurements as well as the volume and subsequent burn rate and efficiency. The results of these measurements applied to ISB in ice fields will be shown. We will also describe our initial efforts to transition these measurements to ROV, autonomous underwater vehicle (AUV), and drone platforms.

2. Method for determining the volume of burning oil

To perform the ISB at our laboratory, we burned the oil on top of water in a small tank as shown in Figure 3. To benchmark the volume of oil removed during burning, the burn rate, and the efficiency, the tank was placed on top of a scale as shown in Figure 4. Multiple visible and IR cameras surrounded the tank at various locations. The data collected to calculate the area from the image analysis and the thickness from the acoustic measurements was synchronized by ensuring the clocks on the two separate computers were synchronized and the start time of the data collection commenced simultaneously. To confirm synchronization several visible markers in the data were used such as the start of the burn or the time when the burn first moved over the thermocouple tree.



Figure 3. Outdoor burning setup at ARA VIMS facility. Photo: Donglai Gong



Figure 4. ISB tank on scale (outline shown in purple).

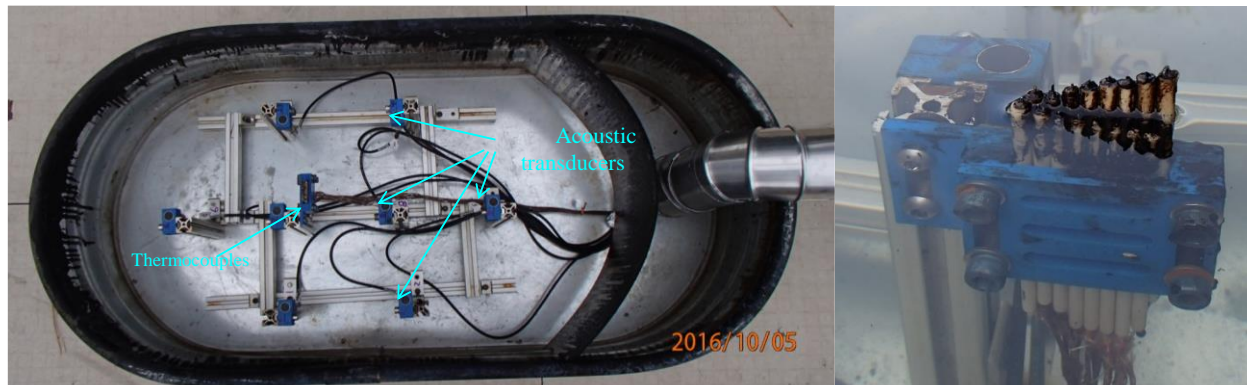


Figure 5. Inside image of the tank with eight ultrasonic transducers and thermocouples (left). Thermocouple tree and acoustic transducer mounted in blue plastic holders (right).

To measure the slick thickness, eight acoustic transducers with a center frequency of 2.25 MHz were placed in the water below the oil slick as shown in Figure 5. The temperature inside the burning slick was measured by 16 thermocouples separated by 1 mm vertically through the depth of the slick and into the water. Each thermocouple was inserted into a ceramic tube and sealed with ceramic cement to protect them from the excessive heat. A close up view of the transducer mounted in a blue plastic holder is shown in the right image along with the thermocouple tree.

2.1. Surface Area of Burn

For computing the surface area of the burn, six machine vision visible light RGB cameras and four long wave infrared (IR) cameras were used to collect the raw imagery.

The RGB machine vision cameras are model UI-5240-SE by IDS, 1024x1280 pixels. They are gig-E standard cameras, which can be completely controlled over Ethernet and programmed via a custom interface to take imagery in an automated manner and immediately make it available to the area algorithm.



Figure 6. Visible and infrared (IR) cameras.

The long wave IR cameras are model 320 from Tamarisk and employ Microbolometer uncooled technology. They have a pixel count of 320x240 and can also be controlled over Ethernet and programmed via a custom interface.

The cameras were mounted inside a rugged enclosure and provided power and network connectivity through cable jacks (Figure 7 and Figure 8). For this work, we used two methods for collecting imagery. The first method, which occurred for the first burn at ARA, the WPI burn, and the first CRREL burn, was to save full resolution stills from each camera as fast as possible. The fastest rate using this process was two seconds but concentrated all the failures in the mini network always to the same camera, which resulted in a decimation. The second method (used throughout the remainder of the project) was to stream a 640x512-resolution video at 17 frames per second. This video streaming process was robust and was able to capture all images for the six RGB cameras.

For the IR cameras, we used saved still images at full resolution with a software trigger for all experiments. This process yielded imagery every two to three seconds for each camera.

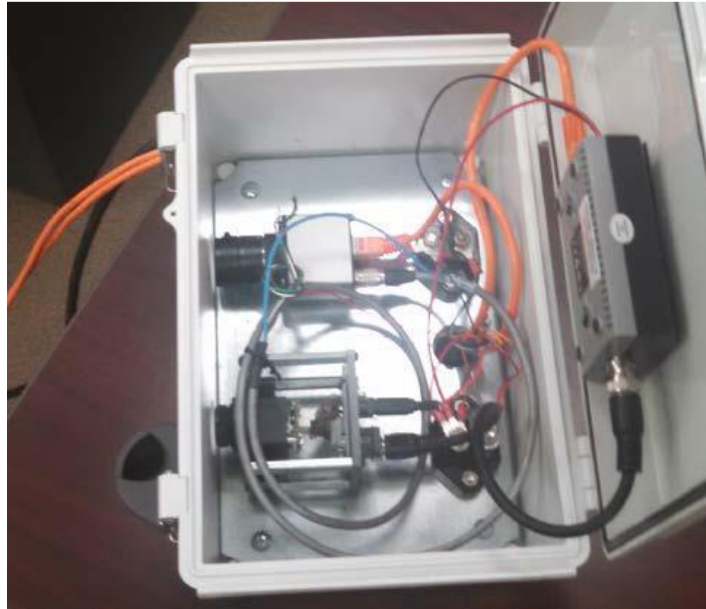


Figure 7. Enclosure for the visible and IR cameras.



Figure 8. Electrical connections for the power and Ethernet.

2.1.1. Area Computation

The burn area was dynamically computed from two or more images and from cameras with varied positions and heights around the fire. The algorithm developed in this project is well suited for automated real-time area computation in open water burning operations. Open water burn volume is typically recorded based on computing the entire burn area in

time and using known oil consumption rates to yield a total burn volume. The automation of the process of area computation and the ability to combine the imagery from any camera can significantly increase the accuracy and reduce the load on humans in the critical moments of a response scenario.

The area estimation method works better at larger scale but was refined in micro burn and small burn situations. These small burns created number of challenges relative to large scale burns including the burns move faster across the field of view, the shape of the burn changes at a faster rate, and close-up fire texture has some transparency and gaps when looking at the burn up close. The transparency and gaps can look like no burning is taking place in a single still shot but should still be counted as burn area. Also, in our lab settings, the burn vessel walls obstructed the view of a larger percentage of the burning area relative to what one would expect from boom in open water. Despite these issues, the algorithm development progressed well and the area computation functioned well in all of our test burns.

The most controlled and confined of the burns that took place at the ARA facility were in a small water trough, which was modified to allow highly instrumented burning including continuous weighing of the entire apparatus. The active burn area of the tank is shown in Figure 9.

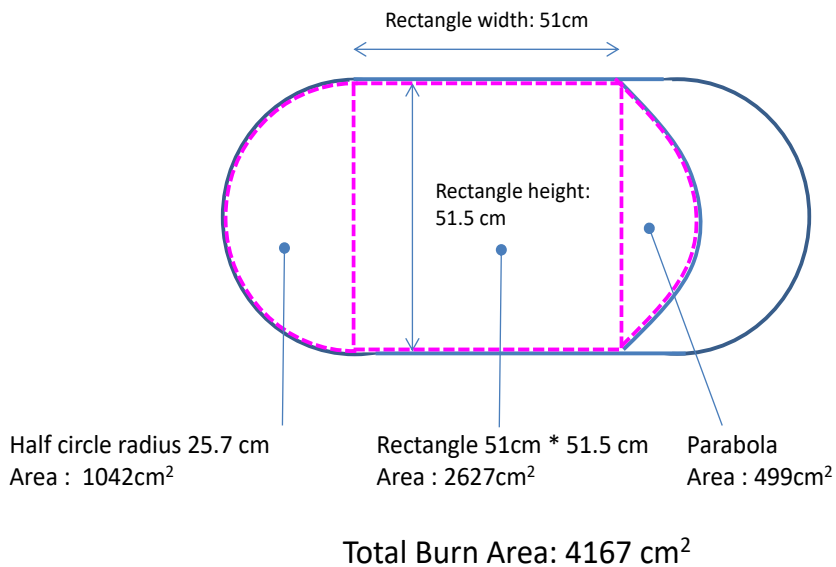


Figure 9. Area of small burn tank used at our ARA-VIMS burn facility.

The test apparatus was excellent for characterizing oil burning behavior and measuring the burn rate because the oil was confined to the prescribed area for most of the burn, and the oil had a fairly uniform thickness over the vessel for most of the burn. In this setting, the area computation was mostly used to track when 100% burning occurred, as the fire moved quickly across the vessel upon ignition and died out just as quickly as the oil reached quenching thickness over the entire area at about the same

instant. Shown in Figure 10 is a plot of the area for such a burn created from the camera images.

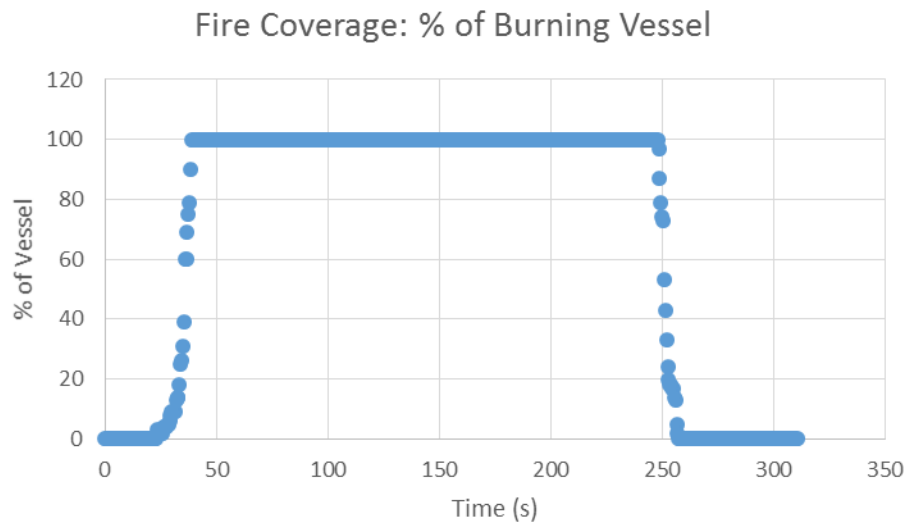


Figure 10. Burn area for ANS oil (April 2017 Burn 16 at VIMS).

The time scale on the area plot is relative to the start of the acoustic thickness and thermocouple data logging data. In this case, the area follows a relatively simple pattern. Occasionally, the burn area lingered at 10% to 80% of the chamber for prolonged periods and in this case, the area data was needed to complete the burning consumption rate computation.

A snapshot of the fire dying out across the burn area and showing approximately 40% to 50% coverage is shown in Figure 11 and will be used to describe the automated area measurement process. The top row of Figure 11 shows the base images taken from three angles around the fire. One image, on the left, misses some of the fire, which is handled by the process. The second row of Figure 11 shows each image from a birds-eye view reference frame. This projection was done by using a planar homography, which warps the image so that a single plane is re-projected to another view angle. This type of transform perfectly preserves the relative geometry for that specific plane but distorts the rest of the image. In this case, the plane of the water is the plane of interest and is projected to the birds-eye view from all images in order to spatially align the data. A computer algorithm then interrogated pixels from all images and determined the burn area. This process was refined so that area could be calculated in real time with sub second time resolution.

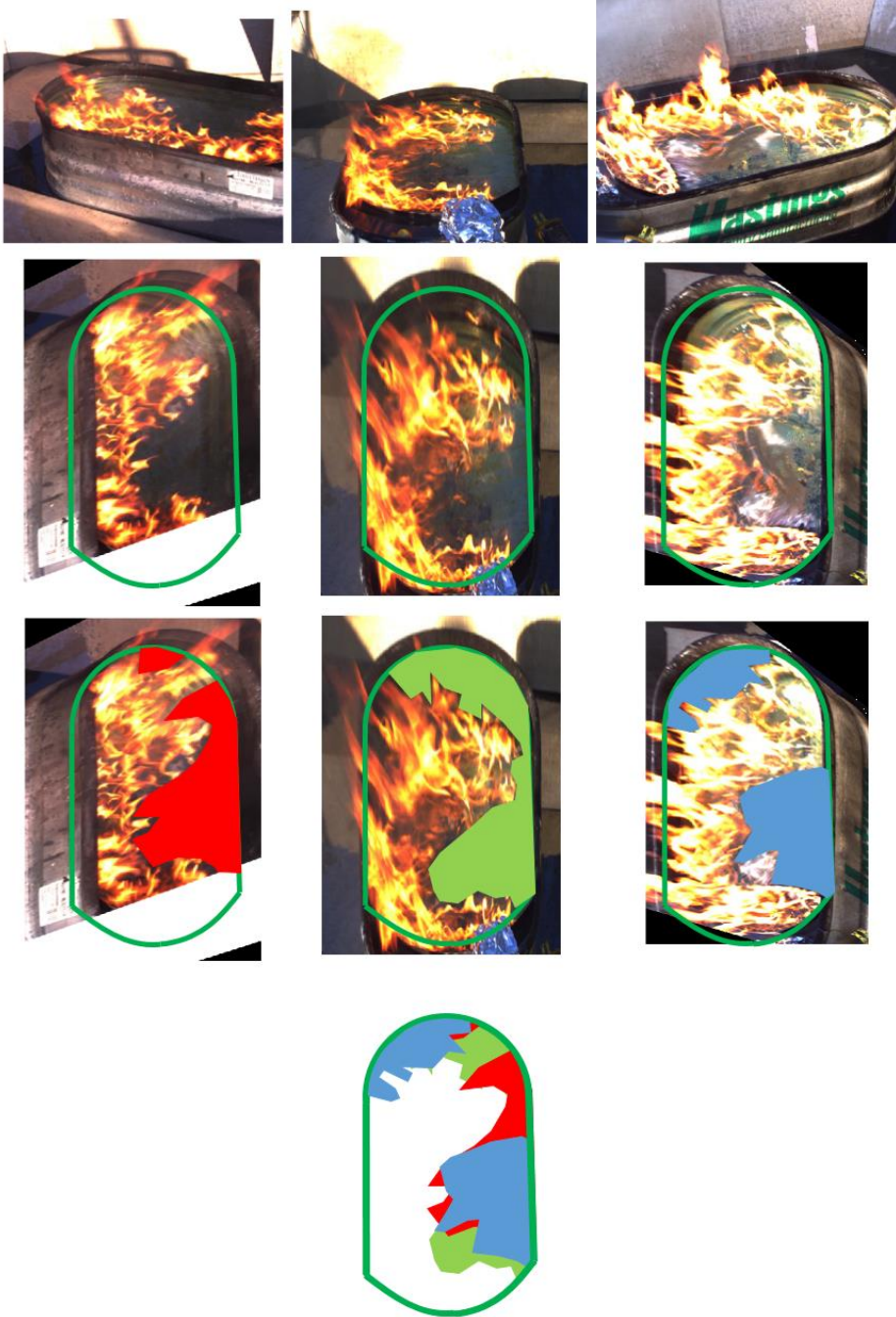


Figure 11. Early version of automated area computation process. Row 1: Imagery from around fire. Row 2: Planar homography to birds-eye view. Row 3: Computer identification of no fire. Row 4: Combine non burning area, count of pixels in white area to yield % burn.

The second-row images shows the part of the fire that rises up off the water, being out of the plane, the fire folds over other parts of the view based on the original angle of the photo. In some cases/viewpoints, the fire obscured non-burning areas behind it. For any region of one of the aligned photos shows absence of fire, then that area can be counted

as fire free. The third row of images shows the fire-free region for each rectified view. The solid colored region is the no fire region for each image. The early version of the algorithm here was a sparse point cloud that was traced by hand and filled for presentation purposes, see Figure 56 for a more mature version of the algorithm automatically filled in through dilation without any touchup. The last row shows all images combined to identify the burn region shown in white.

The steps to make this process work automatically are:

1. Collect images from multiple cameras.
2. Choose a set of images in an appropriate time window to use for the computation.
3. Compute the homography matrix for each image.
4. Project the images to the birds-eye view using the homography matrix (called orthorectification in mapping).
5. Rotate and scale the images to further align them if needed.
6. Detect fire or detect absence of fire in each image. Set fire locations to '0' and non-burning locations as '1'.
7. Fill or dilate region of no fire, more up to date algorithms use multiple images in time superimposed and have few pixel holes to fill.
8. Add all the image overlays spatially. Pixels equal to '0' are locations of fire. The ratio of '0' pixels to overall pixels is the fractional burn area.
9. Supply an external length scale to pixel separation, use boom markers or any known object in the scene or use geotagging of images, and the intrinsic and extrinsic camera parameters.

These steps define the general strategy for burn area computation, which lends itself well to automation, especially for a heterogeneous collection of cameras. In an operational environment where some of the cameras are on the ship deck, some on unmanned aerial vehicles (UAVs) or planes for a large scale burn, there are multiple ways to execute these steps in order to fully automate the process.

2.2. Thickness measurements using acoustics

Measuring the slick thickness using acoustic waves hinges on the ability to distinguish the reflection from the oil-water interface. The strength of the reflection from the oil water interface is controlled by the difference of acoustic impedances of the water and the oil. The acoustic impedance, Z , is given by $Z = \rho V$, where ρ is the density of the fluid and V is the speed of sound in the fluid. The reflection coefficient from the interface of two fluids, R , is given by the following equation.

$$R = \frac{Z_{water} - Z_{oil}}{Z_{water} + Z_{oil}}$$

If the acoustic impedances of the water and oil are equal, then there will be no reflection from the water oil interface. For the oils and temperatures used for this study R ranged from ~ 0.1 at the cold temperatures near 0°C at CRREL to ≥ 0.3 during burning.

Acoustic signals from the oil slick are shown in Figure 12 along with a schematic of the measurement sensor and slick. The data on the right side show the reflections from bottom of the slick, the top of the slick, and a reverberation inside the slick. To calculate the thickness of the slick, we measured the difference in transit time between the top and bottom of the slick using the equation below.

$$Thickness = \frac{\Delta t V(T, t)}{2}$$

Here Δt is the difference in the transit time between the bottom and top of the slick and $V(T, t)$ is the speed of sound in the slick as a function of temperature, T , and time, t . The factor of 2 accounts for the round trip through the slick. Care was taken to ensure the transit time was calculated from peak of the same cycle in each reflection when the shape of the waves were well formed.

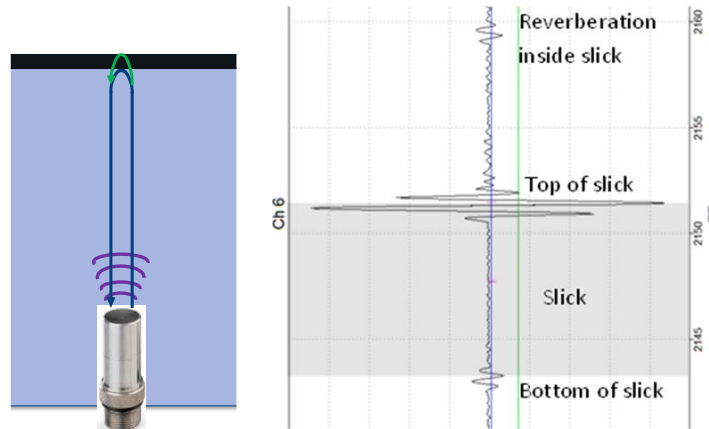


Figure 12. Schematic of acoustic measurements of slick thickness and accompanying data.

A plot of a series of acoustic signals from an oil slick during burning is shown in Figure 13. Each vertical line in this sonar-like image is an individual “ping” like the one shown in Figure 12. The vertical axis is the travel time from the sensor to the slick and back and the horizontal axis is the measurement time. A high acoustic amplitude is red and a small amplitude is black. Before the oil was ignited, the reflection from the bottom of the slick can be seen approximately $20 \mu\text{s}$ from the sensor, the reflection from the top of the slick was approximately $37 \mu\text{s}$ from the sensor, and a reverberation inside the slick can be seen at about $52 \mu\text{s}$ from the sensor. For this burn, the ANS crude oil was ignited at approximately 40 seconds after data collection started. After that time, the travel time increased because the speed of sound in the oil decreased as the temperature rose. This behavior will be described in detail in the next section. The signal from the bottom of the slick stayed stable until about 175 seconds when the water began to boil and evaporate. The top of the slick fluctuated up and down as the oil burned and components of the oil boiled off causing the travel time from the top of the slick to fluctuate in time (vertically). When the water reached 100°C , it began to boil over, causing both the reflection from the top and bottom of the slick to fluctuate dramatically in time and amplitude. During this boil

over, the top and bottom the slick were less distinct. Even with the fluctuations, the time difference between the echoes was easily measured with high accuracy and precision. While interesting, in the open water, boil over is not expected because of the constant movement of the water under the burning oil.

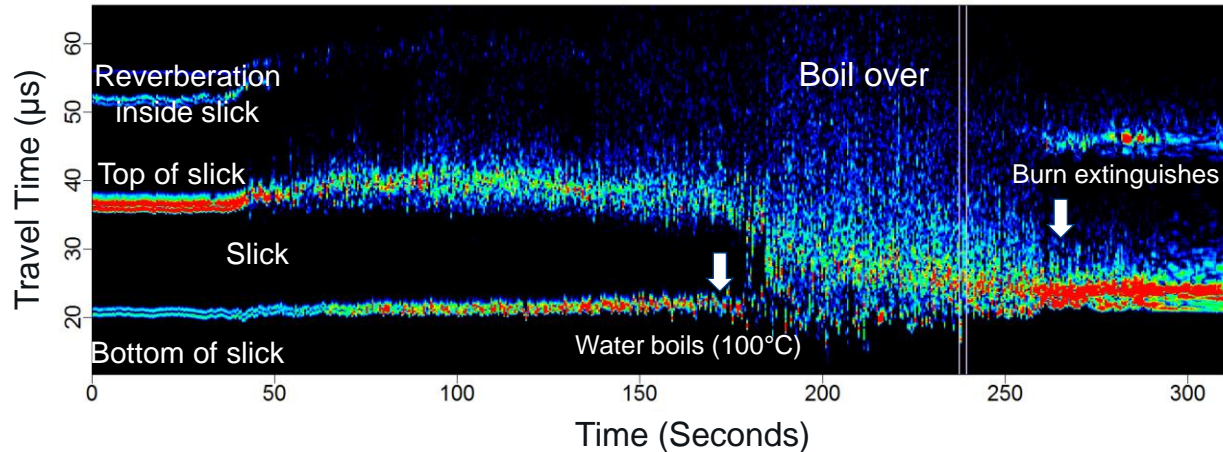


Figure 13. Sonar-like acoustic image showing the reflections from the ANS slick surfaces during ISB.

It is important to notice the large amplitude of returned signal (backscatter) during the burning especially during the boil over when liquid water and oil were ejected into the air. The backscattering is likely caused by acoustic energy scattering from the undulating surface and droplets of liquid as they are ejected from the surface as the liquid boiled. This behavior is most evident during the boil-over phase from ~180 seconds through ~260 seconds as indicated by the high degree of scattering and large amplitude signals during that time frame. The high degree of scatter and movement of the surfaces had little effect on our accuracy and precision of thickness measurements as can be seen in Section 3 where the accuracy and precision of the thickness measurements are discussed.

Qualitatively, this sonar image provides a tremendous amount of information about the dynamics of the burning oil; however, much more useful information can be obtained by measuring the thickness of the oil directly. To determine the thickness of the oil from these measurements of the travel time in the slick, we must know the temperature inside the slick and the speed of sound as a function of temperature. Our measurement of these two parameters will be discussed in the next two sections.

2.2.1. Speed of sound in crude oil as a function of temperature

To measure the speed of sound in fluids at high temperatures, we developed the apparatus shown in Figure 14. The oil chamber was fabricated from a 3.5-inch diameter stainless steel tube that was welded onto a 7.0-inch diameter steel plate. The tube was surrounded with fiber insulation and covered with a thermally insulating cap. Thermocouples and an acoustic transducer were inserted through holes in the cap to measure the temperature and speed of sound. To heat the oil, the apparatus was placed on a hot plate. An acoustic transducer mounted on a five-axis positioning system was

lowered through a central hole in the top thermally insulating cap and used to transmit the acoustic signal into the oil and receive the reflection from the bottom of the oil-filled container. This configuration enabled the travel path to remain constant between the transducer and the bottom of the container so that the changes in transit time of the acoustic signal could directly be used to measure the speed of sound in the oil. The travel distance was determined by measuring the time of flight in fresh water using known values of the speed of sound in water. Three thermocouples were mounted in the insulated cap to measure temperatures at different depths in oil. The temperature was digitized by a National Instruments data collection instrument and acquired simultaneously with the acoustic data. The two pictures on the right in Figure 14 shows a close view of the inside of the oil chamber including the three thermocouples mounted through the insulated cap for measuring the temperature in the oil at different depths.

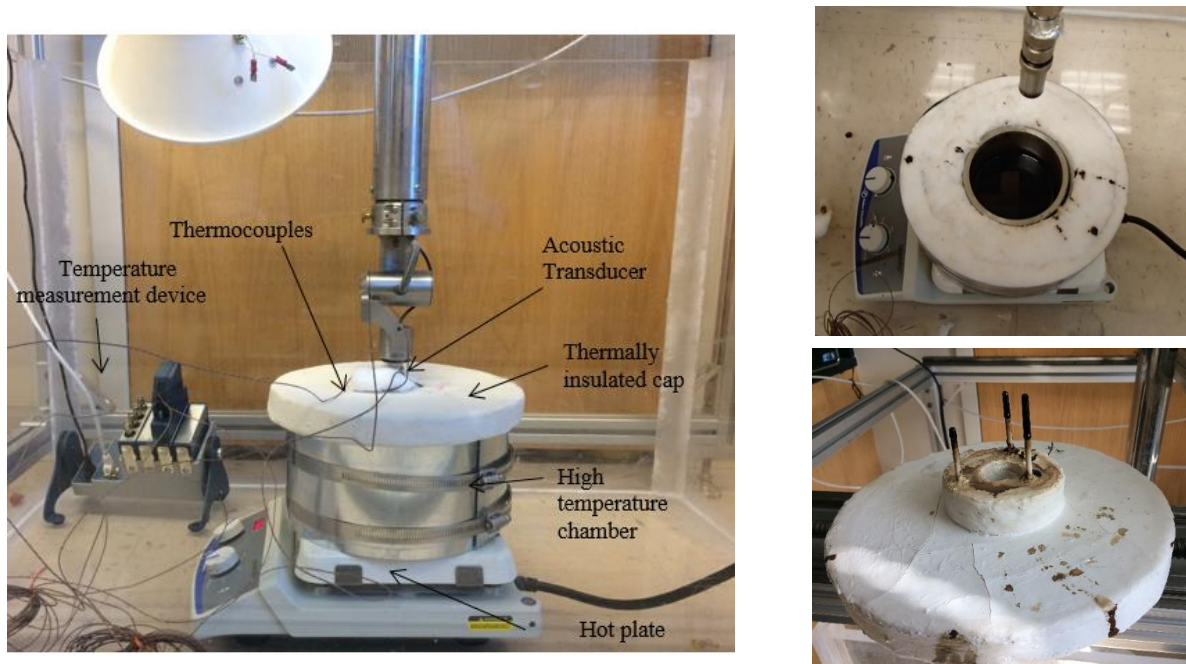


Figure 14. Experimental setup for measuring speed of sound in oil as a function of temperature.

Figure 15 shows the dependence of the speed of sound on temperature from $\sim 20^{\circ}\text{C}$ to 180°C in Agbami, ANS, and Rock crude oils. Data collection was terminated when the oil reached 180°C to ensure that none of the vapors ignited in our enclosed container inside our lab [3]. In the future, we may perform similar measurements in an area where ignition of the oil vapor could be safely performed. The resultant polynomial fit to the data is shown in Table 1.

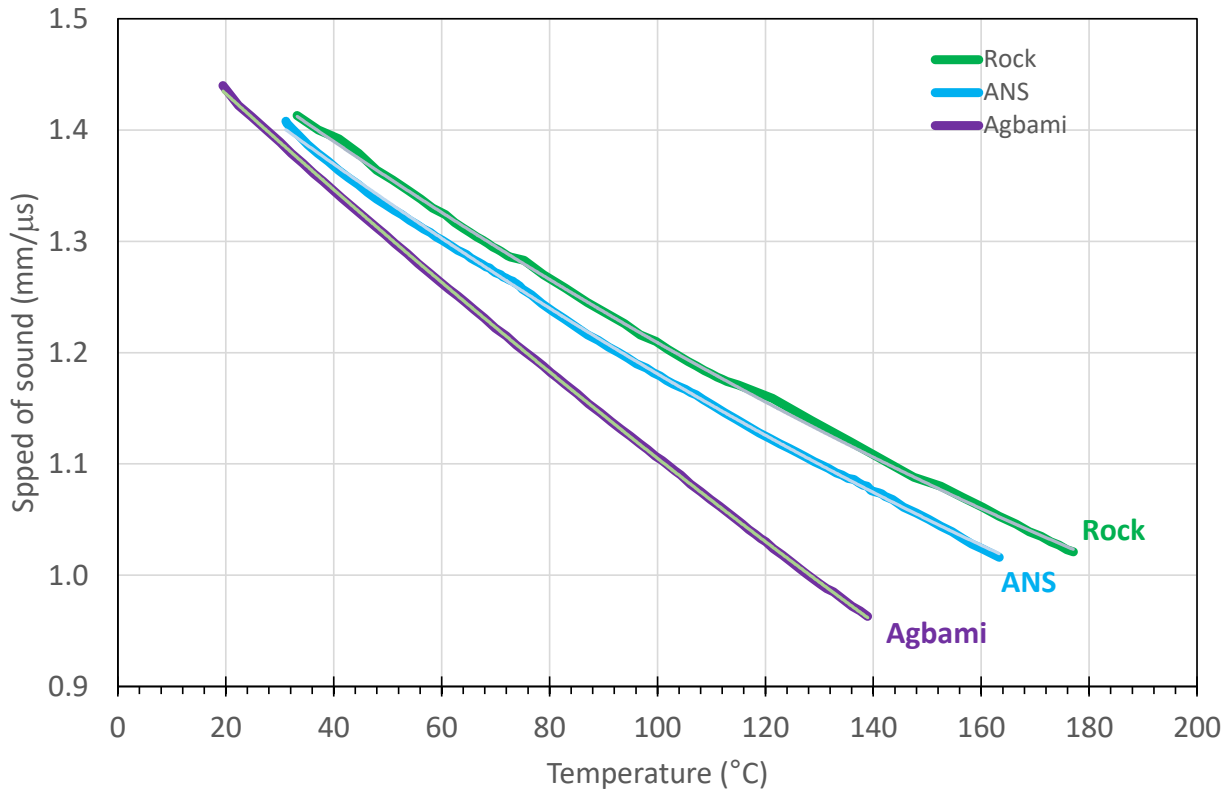


Figure 15. Speed of sound as a function of temperatures for various crude oils used in this work.

Table 1. Speed of sound as a function of temperature

Crude Oil	Speed of sound $V(T^{\circ}\text{C})$ mm/ μs	Classification	Dynamic Viscosity at 20°C (cP)
Agbami	$V = 3.48 \times 10^{-6} T^2 - 4.51 \times 10^{-3} T + 1.52$	Light	2
ANS	$V = 4.41 \times 10^{-6} T^2 - 3.74 \times 10^{-3} T + 1.51$	Medium	25
Rock	$V = 4.35 \times 10^{-6} T^2 - 3.62 \times 10^{-3} T + 1.53$	Heavy	2617

2.2.2. Temperature inside a burning oil slick

As mentioned earlier, the speed of sound in a fluid is a strong function of temperature, which for a burning oil slick changes dramatically from the bottom of the slick, which is in contact with the water, to the top of the slick, which is in contact with the burning oil vapor. To account for the change in the speed of sound, we measured the temperature inside the burning slick and the speed of sound in various oils at temperatures ranging from 20°C to 180°C.

To measure the temperature inside the burning slick, we placed 16 thermocouples separated by 1 mm through the depth the slick. The left schematic in Figure 16 shows the placement of the first 12 thermocouples in a 1-cm thick slick. The right image shows the temperature profile in the burning slick of ANS crude oil shown above. The corresponding depth dependent and time dependence are shown in the two graphs of Figure 17 at the times of the white lines in the temperature profile image. To determine the speed of sound at these high temperatures requires knowledge of the speed of sound in oil as a function of temperature. To determine the temperature dependence of the speed of sound in various oils, we measured it directly in our lab as described in the next section.

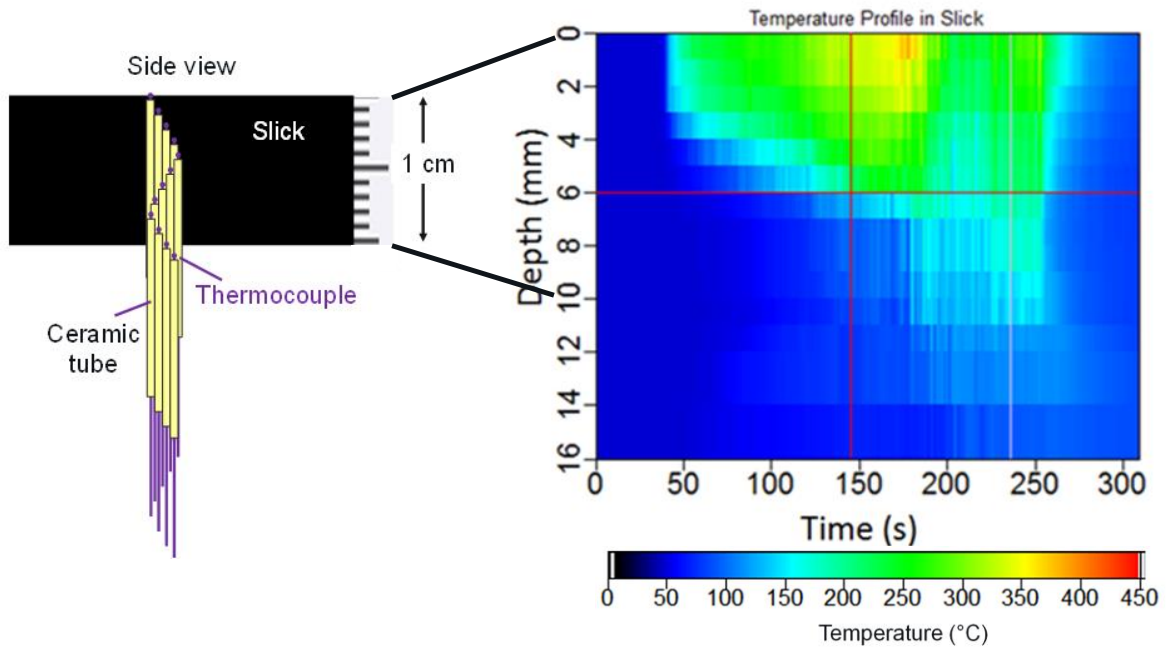


Figure 16. Schematic of thermocouple positions and time-depth temperature profile of ANS burn.

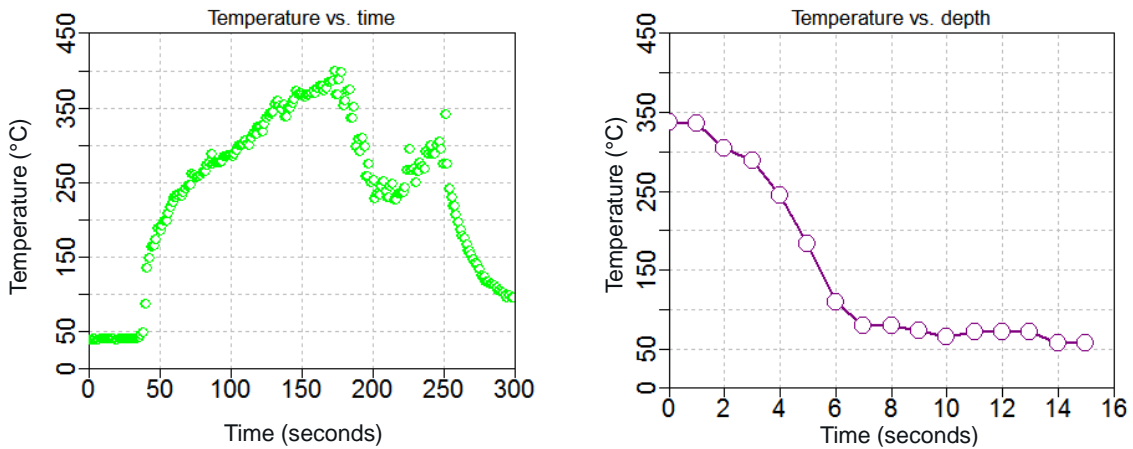


Figure 17. Temperature in a burning slick of ANS as a function of time 1 mm below the initial surface of the slick (left) and as a function of depth at 125 seconds (right).

2.2.3. Thickness measurements in a burning oil slick

The speed of sound during ISB was calculated using the measured temperature and relationship between the speed of sound and temperature shown in Table 1. The temperature profile and resultant speed of sound profile in the slick are shown Figure 18. To calculate the thickness of the slick where a large temperature gradient exists and thus a large gradient in the speed of sound, it is appropriate to use the harmonic mean of the speed of sound. The harmonic mean takes into account the sum of time it takes for the acoustic wave to pass through each layer [4]. For this case, each layer is assumed to be 1 mm thick and it is assumed the speed of sound is constant in that 1mm thick layer.

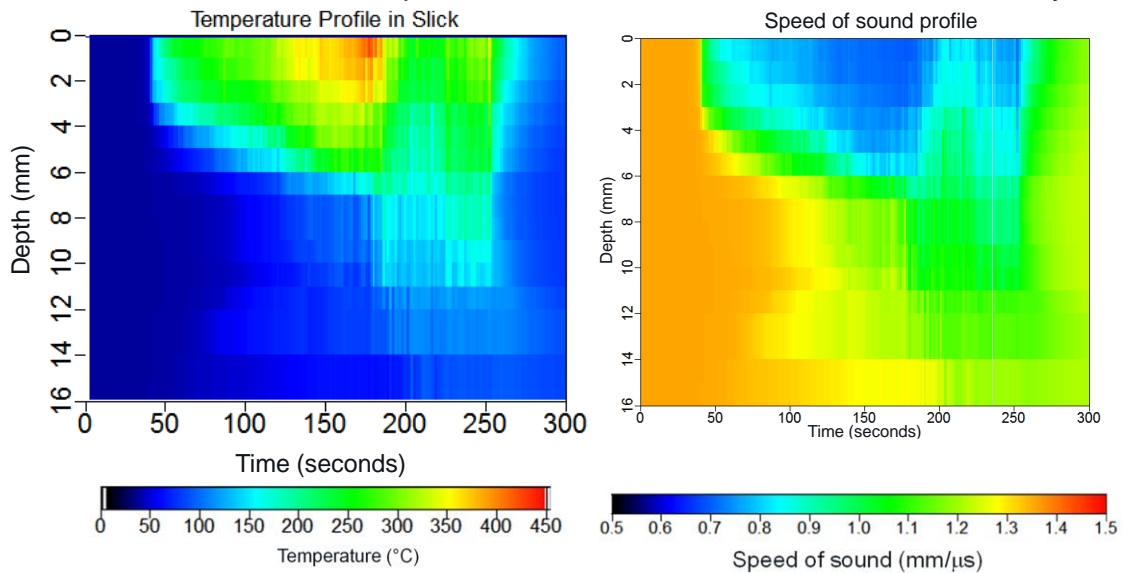


Figure 18 Temperature and speed of sound profiles in a burning slick of ANS oil at ARA-VIMS in 2017.

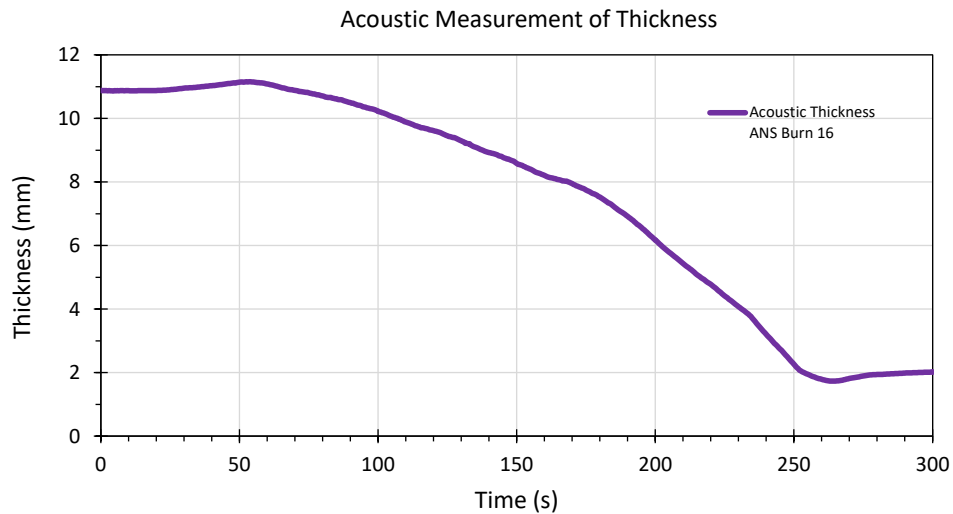
Simply using the harmonic mean to calculate the average speed from the profile in Figure 18 is not adequate. One must also account for the diminishing slick thickness so that the harmonic mean of the speed of sound is calculated over the correct spatial region that encompasses the slick as it burns.

To independently determine the spatial region for calculating the harmonic mean of the speed of sound, the thickness of the slick calculated from the acoustic travel time measurement during burning was compared to the thickness of the slick calculated from the weight loss, area, and temperature dependent density during burning. The weight of the oil during burning was determined by placing the entire burn apparatus on a scale as shown in Figure 19. The scale had a maximum range of 500 pounds (227kg) with a resolution of 0.01 pounds (4.5g) which allowed measurements of ~0.015 mm of oil loss for the given surface area.



Figure 19. ISB tank on scale (outline shown in purple).

For these calculations we performed a minimization process between the thickness from the acoustic transit time measurements (using the harmonic mean of the speed of sound) and the weight calculation at each moment in time during the burn. The assumption is the thickness from each calculation should be the same. The controlling parameter that was allowed to vary in this iterative optimization process was the number of thermocouples used to define the temperature profile for both the speed of sound calculation and the density calculation. The thermocouple range then defined the cutoff temperature which was used to exclude thermocouples from the temperature profile calculation and thus the speed of sound profile. The results for ANS are shown in Figure 20 where the thickness during the burn is shown as well as the maximum cutoff temperature. The most relevant times are during active burning from ~50 seconds to ~250 seconds. To adequately answer the question about the constituents in the oil during burning it would be useful to analyze the components of the oil at various temperatures and times during the burning.



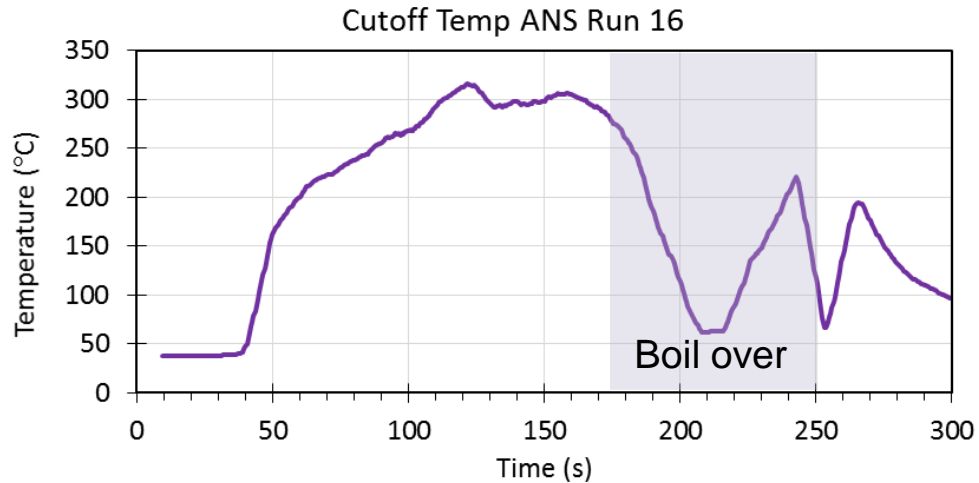


Figure 20. Acoustic measurement of thickness and associated cutoff temperature.

The cutoff temperature distribution is a quantity that has a similar amplitude and pattern within multiple burns of the same oil. The differences in this pattern between oils indicate the cutoff temperature carries fundamental information about the oil. For instance, Figure 21 shows cutoff temperatures for Agbami, ANS, and Rock as a function of time during the burn. The cutoff temperature is used to indicate the top surface temperature in the liquid oil, and shows a much hotter temperature for ANS than for Agbami. Agbami is a lighter oil and has a lower boiling temperature and for this reason will transition to vapor at a lower temperature than ANS and Rock, which has the highest cut off temperature of almost 400°C.

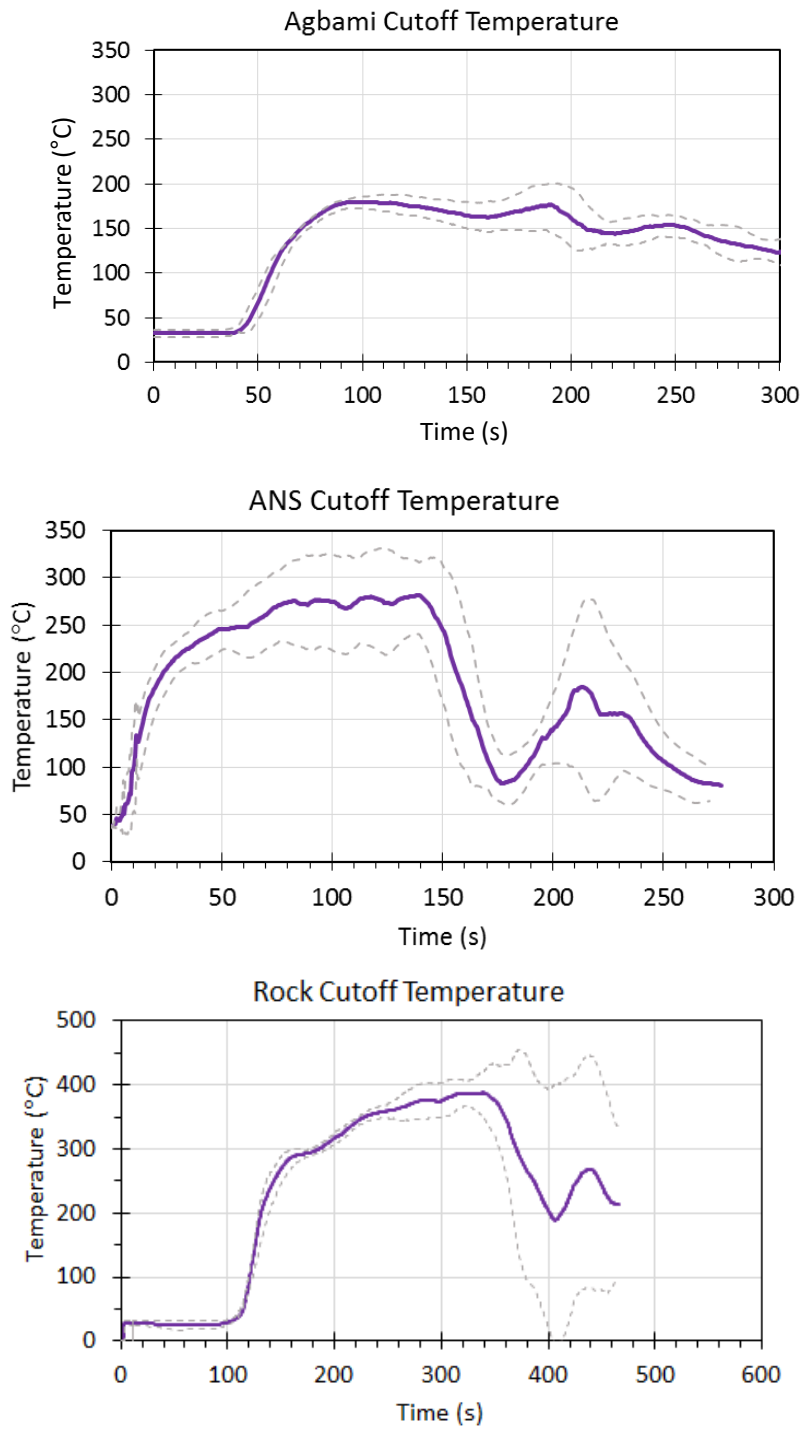


Figure 21. Computed ANS cutoff temperature and Agbami cutoff temperature from three averaged tests shows pattern unique to both oils.

2.2.4. Validation of thickness measurement

The acoustic measurement of thickness was computed by varying the thermocouple range until the density, volume based thickness computation matched with the acoustic based thickness using the harmonic mean of the speed of sound as a function of temperature at each moment in time. The average ANS cutoff temperature shown in Figure 21 was computed from three nominally identical burns. This average cut off temperature (blue) was then used to model other ANS burns as shown in Figure 22 for ANS. For this particular burn we also present the result from measurements the optimization method with the density, volume measurement of thickness (purple). This comparison was performed to show the reliability of using the average cut off temperature for burns where the weight was not recorded.

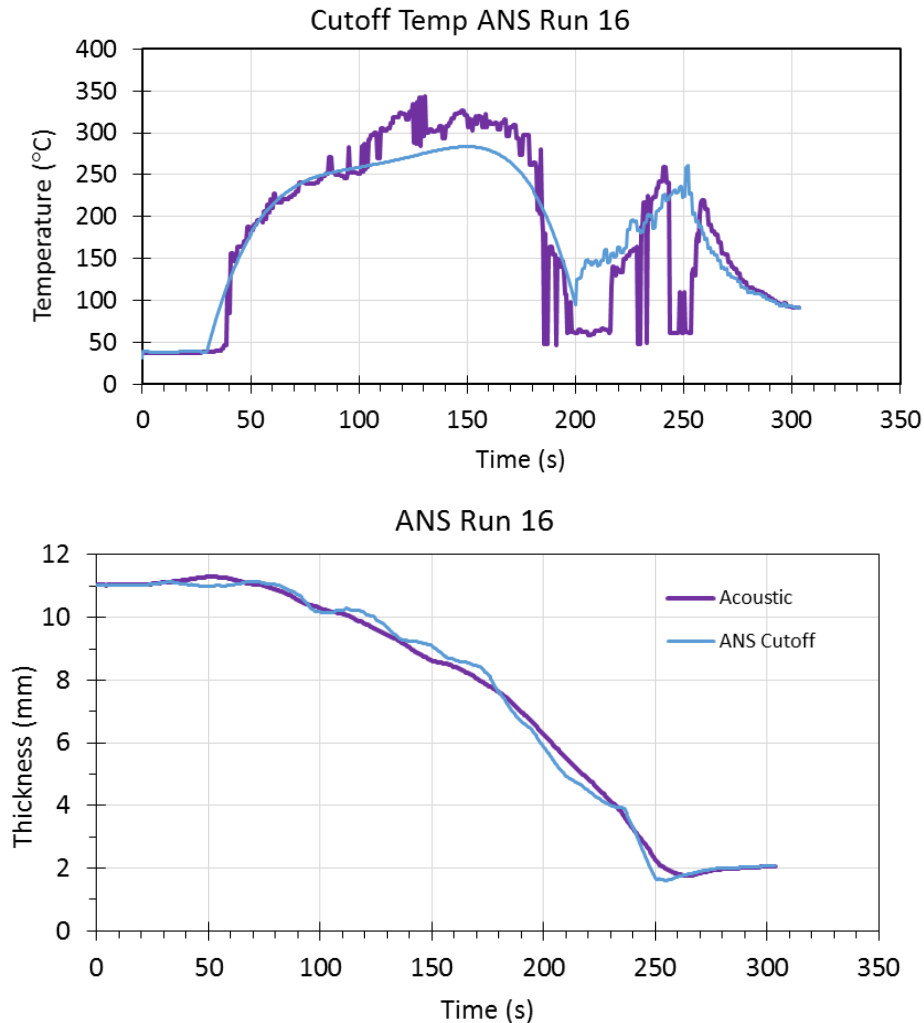
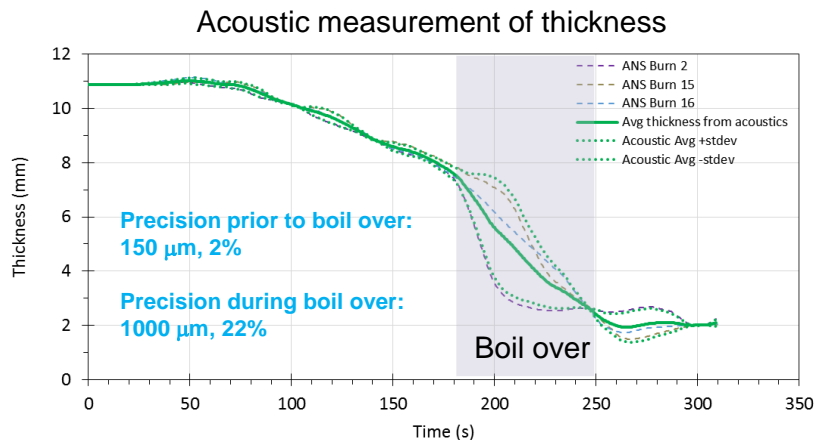


Figure 22. Cut off temperature, curve fit to cut off temperature (blue) and resultant thickness using the “average” ANS cutoff and the measured cut off (blue) and the cutoff for that specific burn (purple).

3. Accuracy and precision of thickness measurements

The thickness from the acoustic and weight measurements agree well and the resultant cut off temperature range is plausible based on knowledge of the fresh oil and the potential changes as the oil burns. To determine the accuracy and precision of the acoustic measurement of thickness and the resulting burn rate, and efficiency, multiple nominally identical burns of ANS, Rock, and Agbami crude oil were performed while weighing the oil apparatus with a scale. The resultant thickness from the validation process for both the acoustic measurement and the weight measurements described in the previous section for three ANS burns is shown in Figure 23 along with the precision reported as plus and minus the standard deviation of the three burns. The reproducibility prior to boil over for the acoustic measurement of thickness is very good resulting in a very high precision of 150 μm (2%). During boil over the standard deviation was much higher likely due to the ambiguity in determining the travel time between surfaces that were less defined and rapidly fluctuating vertically due to the violent boiling processes, resulting in a relatively low precision of 1000 μm (6%). The relatively low precision during boil over is only ± 1 mm which is nearly insignificant for two reasons. First, to the knowledge of the authors, no other technique can measure the thickness of a slick of oil while burning, and second, knowing the thickness of the oil to within 1 mm provides knowledge of the burning oil that previously did not exist before this work. The uncertainty during boil over is also not significant because in the open water, boil over is not expected to occur due to the constant movement of water under the burning slick. In calm waters, one can expect knowledge of the slick thickness to within 150 μm or 2% in this case. For open water with waves, based on our work measuring slick thickness at Ohmsett from a moving ROV platform in waves, without burning, the slick thickness was measured by the team to be 4.6 mm \pm 400 μm in a sea state 3 with waves up to 23 inches from peak to trough [5]. The precision for the density measurements for ANS was very high throughout the entire burn producing a precision of 150 μm (2%) prior to the boil over had 250 μm (6%) during the boil over. These measurements prove the ability to measure slick thickness of burning oil using acoustics with a very high accuracy and precision.



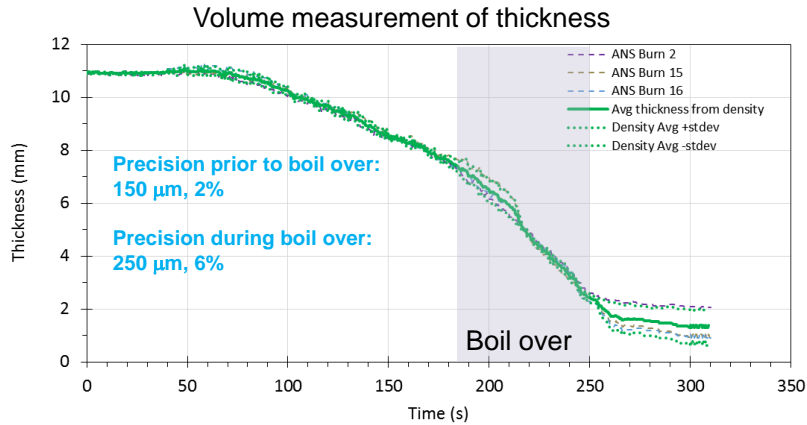


Figure 23. Measurements of the thickness of the oil using the acoustic transit time and harmonic speed of sound (top) and the weight, density, and area (bottom).

To determine the accuracy of the acoustic measurements of thickness, we benchmarked the acoustic measurement of thickness with the measurements from the thickness derived from the weight, area and density. Figure 23 shows the comparison along with the precision of measurements as measured by the standard deviation. Prior to the boil over the average thickness from the two methods are very close and differ only by $310 \mu\text{m}$ (6%). During boil over the difference between the two measurements was higher, but only different by $553 \mu\text{m}$ (11%). Overall for ANS, Figure 25 shows the thickness from the acoustic measurement of thickness vs. the thickness from weight and volume during the burn. Even though the acoustic measurement underestimates the thickness during the boil over, the acoustic measurement is highly accurate, providing a thickness within $310 \mu\text{m}$ (6%) of the thickness based on weight, density, and area. These results show the accuracy and precision of the acoustic measurement of thickness during burning of ANS was quite high and repeatable from burn to burn and prove the ability to measure the thickness of burning oil with acoustic techniques. Using these measurements of thickness, the burn rate of ANS of these small pool fires was 2.1 mm/minute prior to boil over and 3.7 mm/minute during boil over.

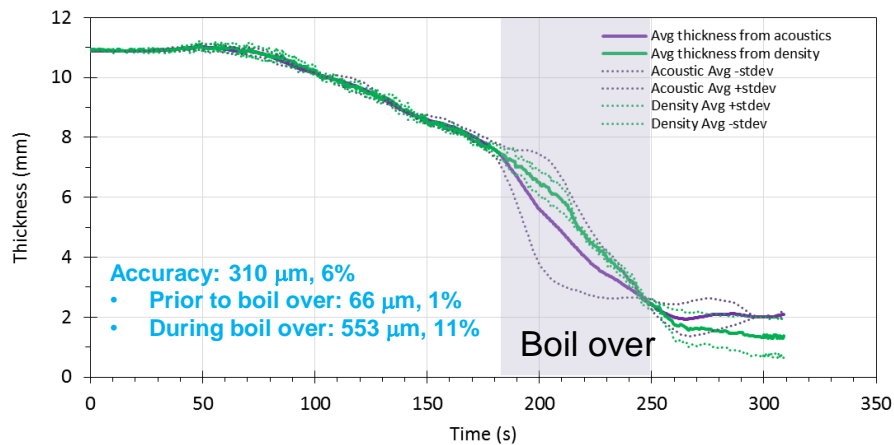


Figure 24. Acoustic measurement of the thickness as a function of time for multiple ANS burns.

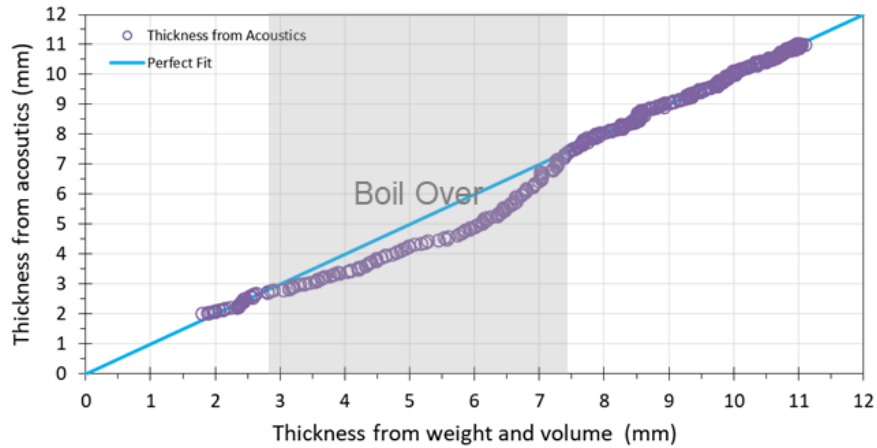
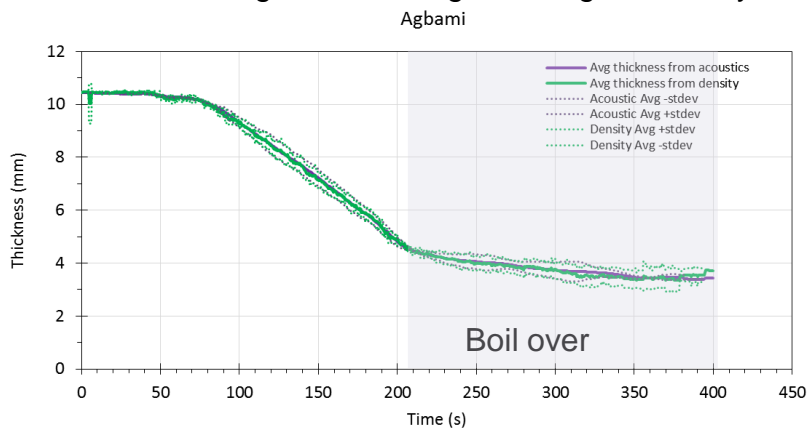


Figure 25. Comparison between the thickness from acoustic measurements and weight measurements of ANS. Agreement is excellent outside of the boil over region.

To show applicability to oils over a range of viscosities we also determined the accuracy and precision of Agbami and Rock crude by comparing the thickness from the acoustic measurements with the direct measurement of thickness from weight loss. The results are shown in Figure 26. This experimental method to validate the thickness measurement contains systematic errors not accounted for here including water evaporation which is counted as burned oil. This method also compares the bulk mass loss measured from the scale with the average of several discrete local thickness measurements thus the error tends to over predict thickness error alone. This measure of error represents the aggregate thickness measurement from multiple transducers as used in all the burns of this study. The resultant accuracy and precision are shown in Table 2. Prior to boil over the accuracy and precision are quite high showing the ability to measure the thickness to within $\pm 590 \mu\text{m}$ for Rock. These results validate the measurement of the thickness using oils that range from light to heavy.



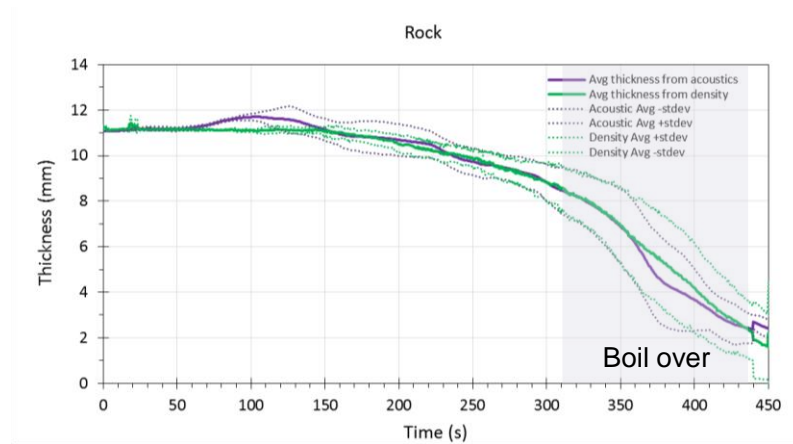


Figure 26. Thickness as function of time for Agbami and Rock determined from acoustic measurements and density, weight measurements for multiple burns.

Table 2. Accuracy and precision of thickness measurements for oils used in this study as computed from the divergence between density, volume computed thickness from scale data and from the direct acoustic time of flight using three burns for each oil

Oil	Dynamic Viscosity at 20°C (cP)	Classification	Accuracy	Precision
Agbami	2	Light	50 μm, 1%: Prior to boil over 72 μm, 1%: During boil over	270 μm, 4%: Prior to boil over 170 μm, 4%: During boil over
ANS	25	Medium	66 μm, 1%: Prior to boil over 553 μm, 11%: During boil over	150 μm, 2%: Prior to boil over 1000 μm, 22%: During boil over
Rock	2617	Heavy	170 μm, 1%: Prior to boil over 370 μm, 11%: During boil over	590 μm, 6%: Prior to boil over 1600 μm, 30%: During boil over

4. Accuracy and precision of area estimate

The error for the area estimate originates mostly from the position and orientation of the cameras. The oblique angle image transformed to the aerial view stretches the pixels to project the shapes as they would be viewed from a normal overhead angle. Along with the stretching of the geometry the corresponding error is also “stretched”. Even though the registration error, the accuracy that specific features in the scene are captured in pixel coordinates, is fairly consistent, the horizontal projection of the error onto the plane of interest gets quite high for oblique angle imagery.

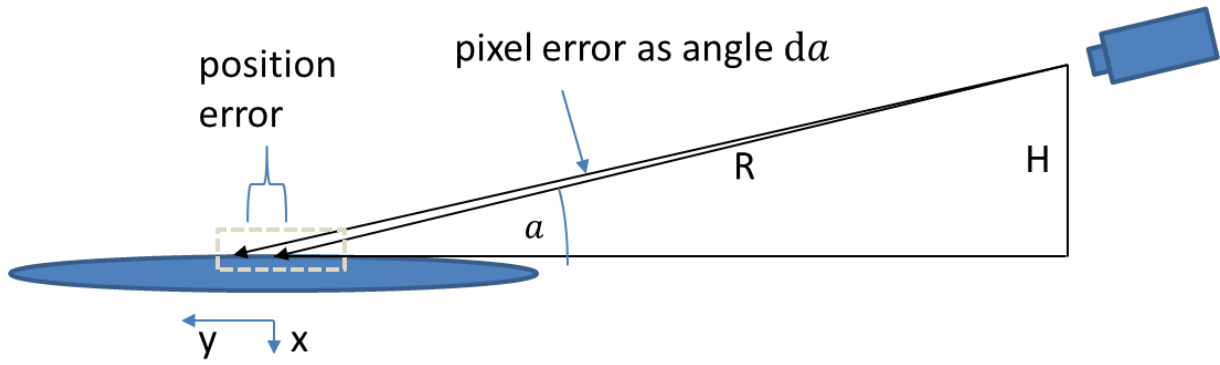


Figure 27. Oblique camera angle to water surface shows projection of angular error to error in y , the horizontal component.

For single fiduciary marks in harsh outdoor conditions it is reasonable to consider the angular error da to be about one pixel [6] for the purpose of determining how the overall error varies with angle a , shown in Figure 27.

In some cases the angle a to the camera sensor will change significantly from the front to the back of the fire. The analysis here will consider the localized angle first, then the overall pattern. The projection of the original image on the sensor is based on the focal length of the lens and the distance to the camera where $y' = f y / |z|$, with z being the distance to the camera, y being the real world coordinate vertical in the image and perpendicular to the camera, and f is the focal length of the camera in pixels. Given the pixel spacing on the camera, the distance on the pond per pixel can be computed.

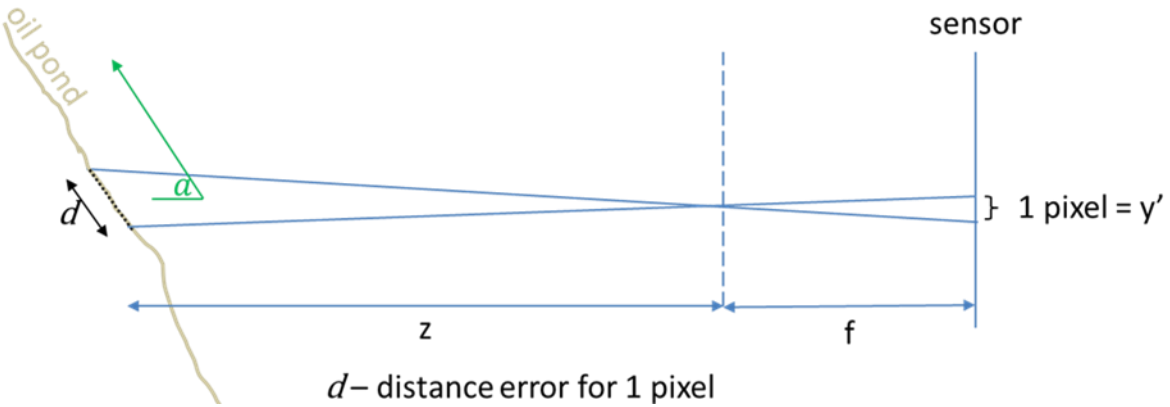


Figure 28. Application of lens equation to estimate 1 pixel error

Using the lens equation as the basis, the distance error for a pixel can be computed,

$$\frac{d \sin a}{z} = \frac{1}{f}, \quad d = \frac{z}{f \sin a}$$

a = angle from tangential

z = distance from camera to target
 f = camera focal length

As z increases the error increases linearly due to the pond looking smaller in the frame, as the focal length goes up the error decreases, only because there are more pixels on the target for a longer focal length. The only real interesting thing here is the relation with the camera angle, a , where the error goes as $1/\sin(a)$. The $1/\sin(a)$ pattern is easy enough to understand, it blows up at small angles and goes to infinity at zero. To scale the curve, the number of pixels from top to bottom of the fire needs to be considered. In this case the aspect ratio, the x to y dimensions of the fire at low angles is limited by the sensor frame. Given a round fire and a 1024 x 1024 camera the horizontal dimension of the camera needs to fit the fire, the vertical direction will see the fire reduced.

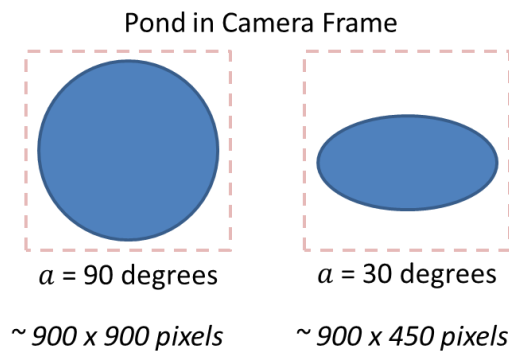


Figure 29. Framing of burn area reducing vertical pixel resolution

Thus, the ability of the camera to frame in terms of how many pixels it can capture in the vertical direction goes as $\sin(a)$. And finally, the total error based on the pixel error and the framing error can be combined to compute the error in the area. The following table computes the error based on the simple fiduciary mark error and then considers an error in the area as a %. The percent error in the vertical direction in the image is applied to two points in the vertical direction so the percent error simply transfers directly to the overall area.

Table 3. Error in area due to registration at oblique angles.

f = 2000 pixels

z = 10 meters

camera resolution = 1024 x 1024

4 meter diameter circular burn 12.56 m²

Angle a (degrees)	Pixels X	Pixels Y	Pixel Error X	Pixel Error Y	% Error X	%Error Y	Area Error m ²
5	800	69.72	0.0050	0.0574	0.0006	0.0823	1.033E-02
10	800	138.92	0.0050	0.0288	0.0006	0.0207	2.603E-03
15	800	207.06	0.0050	0.0193	0.0006	0.0093	1.172E-03
20	800	273.62	0.0050	0.0146	0.0006	0.0053	6.711E-04
25	800	338.09	0.0050	0.0118	0.0006	0.0035	4.395E-04
30	800	400.00	0.0050	0.0100	0.0006	0.0025	3.140E-04
35	800	458.86	0.0050	0.0087	0.0006	0.0019	2.386E-04
40	800	514.23	0.0050	0.0078	0.0006	0.0015	1.900E-04
45	800	565.69	0.0050	0.0071	0.0006	0.0013	1.570E-04
50	800	612.84	0.0050	0.0065	0.0006	0.0011	1.338E-04
55	800	655.32	0.0050	0.0061	0.0006	0.0009	1.170E-04
60	800	692.82	0.0050	0.0058	0.0006	0.0008	1.047E-04
65	800	725.05	0.0050	0.0055	0.0006	0.0008	9.557E-05
70	800	751.75	0.0050	0.0053	0.0006	0.0007	8.890E-05
75	800	772.74	0.0050	0.0052	0.0006	0.0007	8.414E-05
80	800	787.85	0.0050	0.0051	0.0006	0.0006	8.094E-05
85	800	796.96	0.0050	0.0050	0.0006	0.0006	7.910E-05
90	800	800.00	0.0050	0.0050	0.0006	0.0006	7.850E-05

Looking at Table 3 it is clear that the error due to registration technique itself is very small. There are, however, other sources of error to consider. In the open ocean there will be swells that act in the normal direction to the surface. In the lab scale, using the 4 meter by 4 meter burn in Table 3 consider a 13 cm error normal to the plane of the burn to be equivalent to a one meter swell on a 30 meter burn. Again the in-plane error goes as $L = s/\sin(a)$, where the variable are defined in Figure 30.

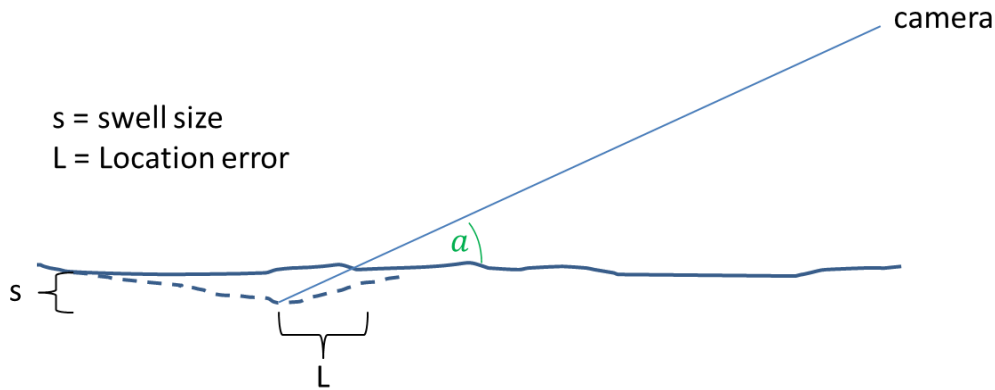


Figure 30. Ocean swell indicated as dotted line translates to error L in planar location.

Now applying a 13cm swell to the 4m x 4m burn shown in Table 3 yields an update table of the error as shown in Table 4. The % error is also plotted in Figure 31.

Table 4. Error from physical shifting of burn plane

f = 2000 pixels
z = 10 meters
camera resolution = 1024 x 1024
4 meter diameter circular burn 12.56 m²
13 cm swell

Angle a (degrees)	Absolute Error Y (m)	Area Error m ²	% Error Area
5	1.4916	5.97	47.50
10	0.7486	2.99	23.84
15	0.5023	2.01	16.00
20	0.3801	1.52	12.10
25	0.3076	1.23	9.80
30	0.2600	1.04	8.28
35	0.2266	0.91	7.22
40	0.2022	0.81	6.44
45	0.1838	0.74	5.86
50	0.1697	0.68	5.40
55	0.1587	0.63	5.05
60	0.1501	0.60	4.78
65	0.1434	0.57	4.57
70	0.1383	0.55	4.41
75	0.1346	0.54	4.29
80	0.1320	0.53	4.20
85	0.1305	0.52	4.16
90	0.1300	0.52	4.14

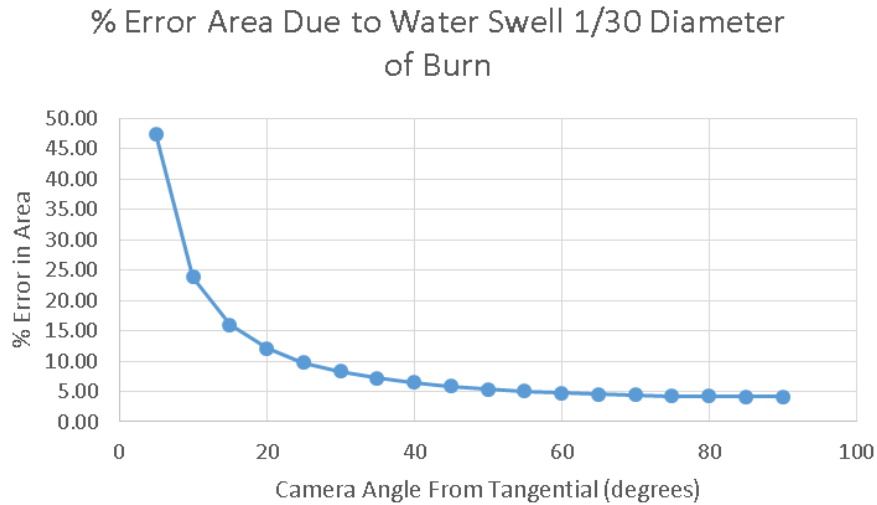


Figure 31. % Area Error as a function of camera angle based on a displacement of the water surface due to wave action or 1/30 the diameter of the burn.

The error analysis clearly indicates that the primary error that needs to be addressed is at low camera angles and come from the body of water containing the burn deviating from a planar shape. Strategies for open water burns must take this orientation and error into account. On the other hand, undue focus on perfecting the fiducial patterns and registration strategies are not merited as the error does not come from these features.

4.1. Multiple Camera Error

The error can be reduced with multiple cameras as the cameras have different incident angles. Since homography errors tend to have specific patterns about the camera axis images coming from multiple directions offer an opportunity to greatly reduce the error.

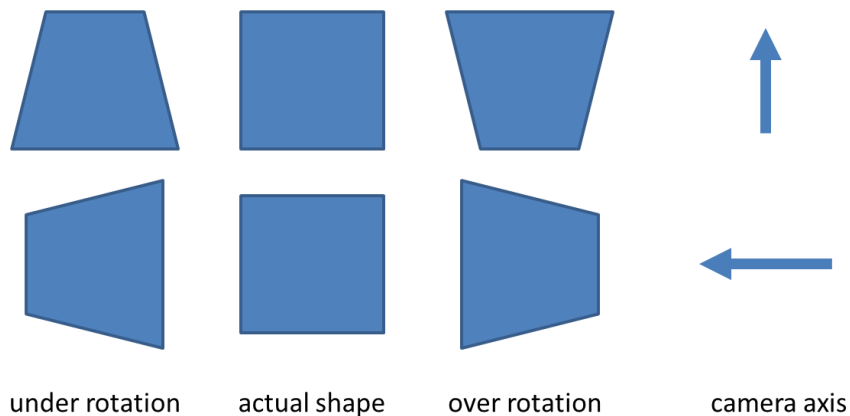


Figure 32. Matching shaped by iterating on rotation of image about the normal perspective.

One example is shown in Figure 32. For illustration purposes a square burning pool is considered. When forming a homography matrix sometimes the points chosen are not perfectly representative of a planar surface. In that case the first application of the matrix creates a set of 'birds eye view' representations that are not totally aligned. The regions at the water fire perimeter typically have a unique shape and lie in the plane of the water. The degree of correspondence between these regions can be used to iterate the homography rotation angle until the perimeters from different images align.

The test image correspondence, and the application of a homography are both very fast operations and can be accomplished tens or hundreds of times in a second. By matching the shape of the perimeter for more than one image the initial error due to homography based on a single set of control points can be greatly reduced or eliminated in this way.

4.2. Strategy For Area Computation

The combined solver technique evolved throughout the project. The final algorithm used the following steps:

1. Apply camera calibration, a simple one parameter radial distortion is adequate. For this project the focal lengths of the cameras are relatively long and the lens setup has little distortion.
2. Assign each camera an angular position around the burn, this position indicates the pose direction the camera has aiming to the fire. This assignment could be achieved with a compass in a dynamic scenario.
3. Use image analysis to establish a tilt angle of the horizontal part of the image, the image needs to be rotated in the x-y pixel plane until the horizon is parallel to the top/bottom of the image or at least balanced left to right.

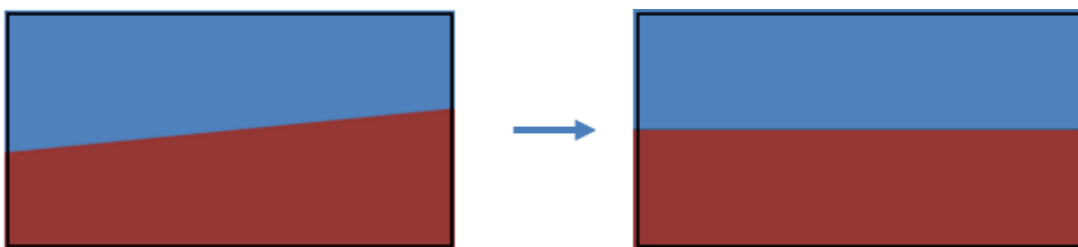


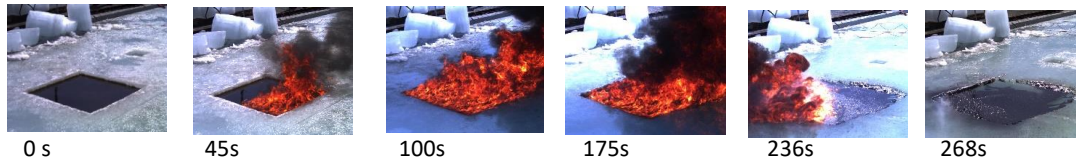
Figure 33. Rotate in image plane to balance horizon.

4. Difference N-images and accumulate the root mean square (RMS) in a single image, this process represents moving elements of the image. Both water and fire will become bright in the composite image. The number of images is an adjustable parameter.

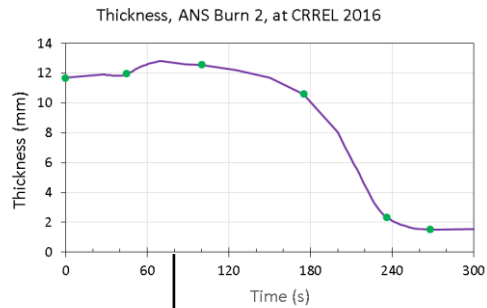
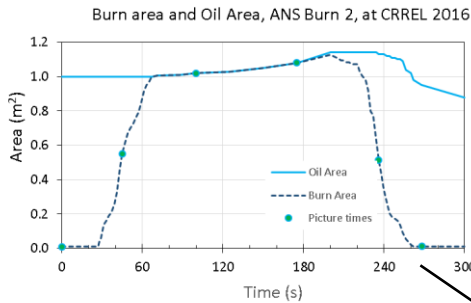
5. Use a base homography given to the algorithm by prior knowledge of the camera tilt angle. If the base homography does not exist construct one based on selected points or instrumentation giving camera pose. For the purposes of the lab experiments the homography was constructed from the camera position.
6. Rotate each image about its first computed birds eyes view in half degree increments in the altitude angle about the zenith ± 3 degrees.
7. Superimpose all images by combining and then normalizing the intensity pattern. Cycle through each individual image and perform an image correlation test to determine agreement with the composite image. Select the image from each camera with the highest correlation to the composite.
8. Optional step. Repeat step 7 forming a new composite using $\frac{1}{4}$ degree increments about the best image for each camera.
9. Store the final homography for each camera and use it as a starting point for the next computation.
10. In the static case step 1 to step 4 will be done pre-ignition.
11. After ignition use step 4 as a starting point, use the saved homography to transform the images.
12. Use the composite fire image against the composite water image to establish fire/no fire regions. Superimpose all images and sum regions of 16×16 pixels which are above a threshold established by taking a midpoint between burn and no burn regions from previous steps. The initial threshold is set as water $R + 50, G + 30, B + 20$.
13. Sum pixels in no fire region and fire region. Use known size of burn vessel to calculate area. Alternate scale/normalization is to use two points of known distance apart in rectified imagery to create pixel scale.

5. Burn rate and efficiency

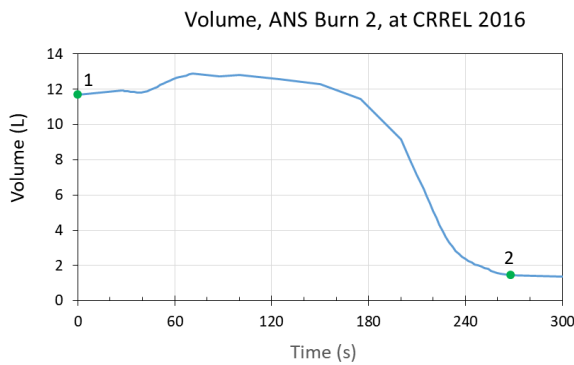
By creating this new capability to accurately measure the surface area and thickness in real time with sub second intervals, we created the unprecedented ability to calculate various properties of the burning slick, including burn rate, to allow the study of various dynamics of the burning oil that could not effectively be studied prior to this work. Using these data we calculated the burn rate as measured by the change in thickness as a function of time. The method used to integrate the area measurement with the thickness measurement to calculate the volume and subsequent burn rate are shown in Figure 34 for ANS at CRREL in an ice cavity with an initial area of 1 m^2 .



melting increases size of ice pocket



$$\text{Oil Volume} = \text{Area} \times \text{Thickness}$$

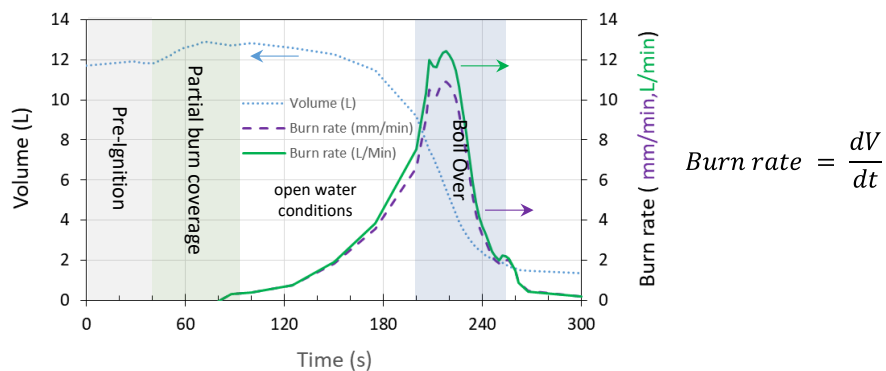


$$\text{Efficiency}\% = \frac{V_1 - V_2}{V_1}$$

$$V_1 = 11.7 \text{ L}, V_2 = 1.4 \text{ L}$$

$$\text{Efficiency} = 88\%$$

ANS Burn 2, at CRREL 2016



$$\text{Burn rate} = \frac{dV}{dt}$$

Figure 34. The combination of area, thickness, volume to calculate the instantaneous burn rate and efficiency.

Table 5 shows the resultant burn rate as a function of time for the multiple ANS, Agbami, and Rock burns. As expected the burn rate is not uniform throughout time since

the burn rate is expected change as the water underneath the oil removes more heat from the oil as it thins [1] and components of the oil burn off. The burn rate during steady burning ranged from 0.6 mm/minute for Rock to 2.7 mm/minute for Agbami. There was a noticeable increase in the burn rate during boil over for Rock and ANS from 0.6 mm/minute to 4.0 mm/minute and from 2.1 mm/minute to 3.7 mm/minute respectively. Interestingly the burn rate for the lower viscosity Agbami decreased during boil over from 2.7 mm/minute to 0.3 mm/minute. The efficiency calculated from these measurements are shown in Table 5. It is expected for ANS that the burn rate and efficiency for large scale burns will be between 80% and 95% [4]. The measured efficiency based on the decrease in volume for these small contained burns fall in that range for ANS and outside that range for Agbami and Rock.

Table 5. Burn rate and efficiency.

Oil	Dynamic Viscosity 20°C (cP)	Classification	Environment	Burn rate before boil over (mm/min)	Burn rate during boil over (mm/min)	Thickness (mm)		Area (m ²)		Volume (L)		Efficiency
						Initial	Final	Initial	Final	Initial	Final	
ARA-VIMS												
Agbami	2	Light	Contained pool	2.7	0.3	10.7	3.6	0.5	0.5	4.9	1.6	66%
ANS	25	Medium	Contained pool	2.1	3.7	10.8	1.9	0.5	0.1	4.9	0.2	96%
Rock	2617	Heavy	Contained pool	0.6	4.0	11.2	2.7	0.5	0.5	5.1	1.2	76%

6. Applications to various ISB scenarios

In addition to developing the capability to measure the instantaneous burn rate and efficiency, we applied the capability to various ISB scenarios including oil in ice fields, different oils, and applications of herders towards the end of the ISB at several sites. The test site at ARA's outdoor VIMS facility was shown previously. In the section that follow, we will show results from ARA-VIMS facility, the Burn Lab at Worcester Polytechnic Institute (WPI) in Massachusetts and the Army Cold Regions Research and Engineering Laboratory (CRREL) in Hanover, New Hampshire. For these measurements we applied the maximum cutoff temperature derived from the validation measurements to calculate the thickness, burn rate, and efficiency. While this method relies on measurements of the temperature inside the slick, it is a first step towards measuring the slick thickness and burn rate in the field where measurements of the temperature inside the slick will not be known.

6.1. Contained burns at the outdoor ARA-VIMS burn facility

The thickness of burning slicks at ARA-VIMS were calculated based on the cutoff temperature derived from the validation measurements shown in Figure 21. For this process we chose one burn of Agbami, ANS, and Rock to test the ability to measure the slick thickness without knowledge of the weight loss. The temperature profile, the temperature 1 mm below the surface, the acoustic “sonar” image of the slick as well as the resultant thickness are shown in Figure 35, Figure 37, and Figure 39 for Agbami, ANS, and Rock respectively. The corresponding area of the burning oil are shown in Figure 36, Figure 38, and Figure 40. The thickness calculated using the average cutoff temperature (labeled cutoff) agrees well with the thickness derived from the optimization process with the weight loss and volume measurements (labeled acoustic) for these three oils. While there is some variation between the two measurements they generally agree implying that the method chosen is potentially in a fruitful direction for dealing with unknown variables expected in the open water. Ideally one would be able to perform the calculation of thickness without knowledge of the temperature, but we have not yet developed that process.

VIMS April 2017: Agbami Burn 5

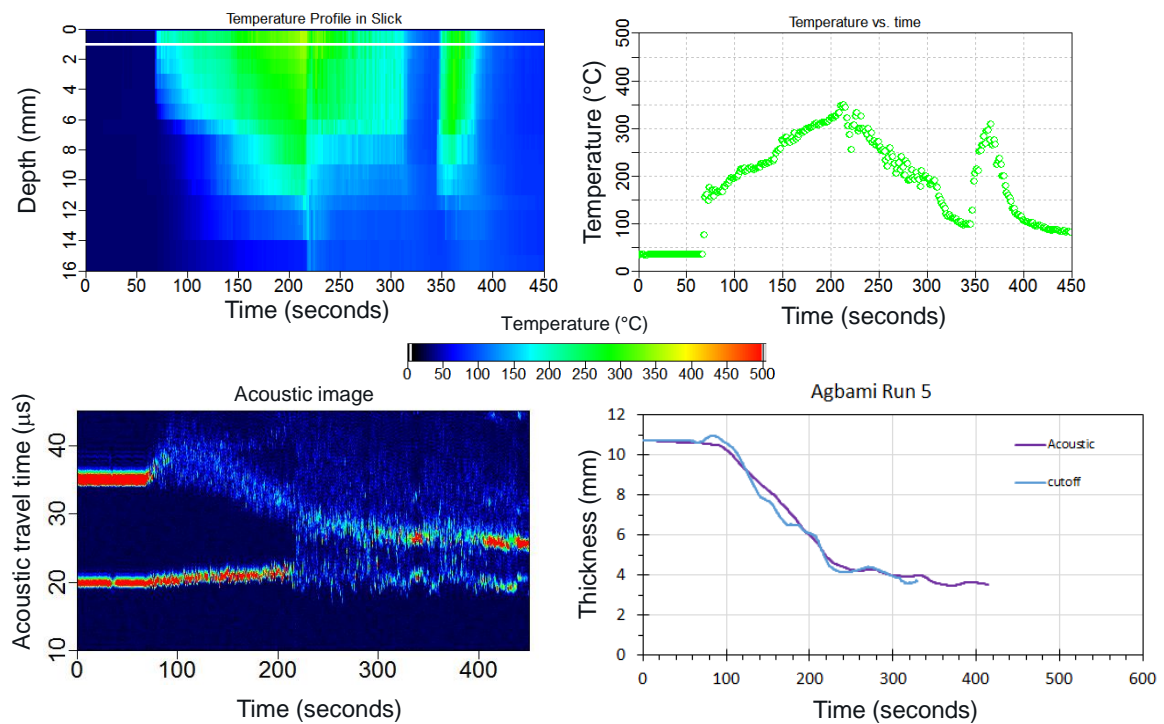


Figure 35. The temperature profile, acoustic image, and resultant thickness for Agbami using the optimization process and the average cutoff temperature.

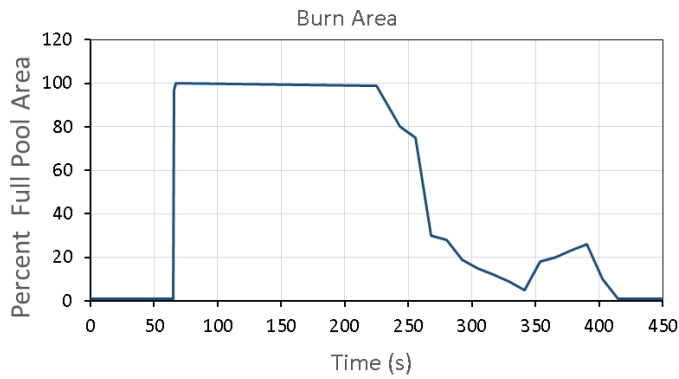


Figure 36. Burn area VIMS Agbami Burn 5

VIMS April 2017: ANS Burn 2

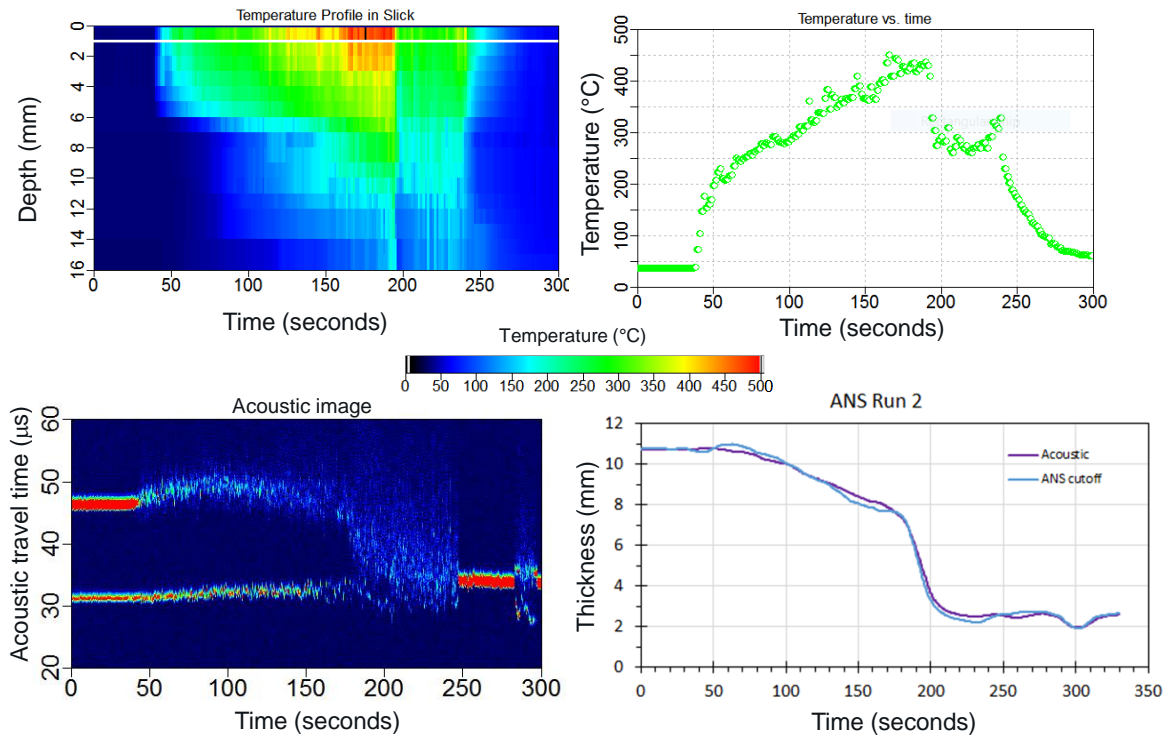


Figure 37. The temperature profile, acoustic image, and resultant thickness for ANS using the optimization process and the average cutoff temperature.

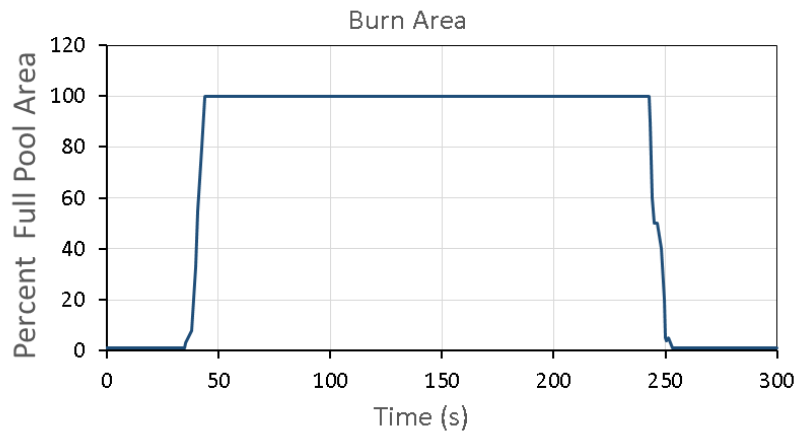


Figure 38. Burn area VIMS ANS Burn 2

VIMS April 2017: Rock Burn 10

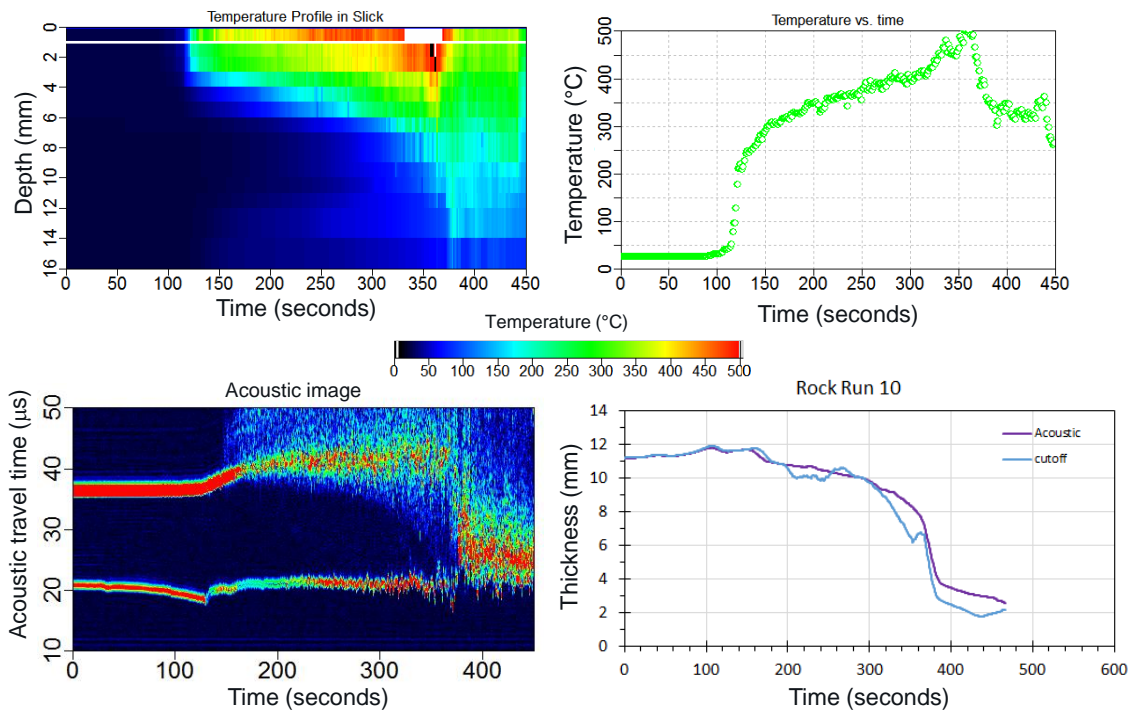


Figure 39. The temperature profile, acoustic image, and resultant thickness for Rock using the optimization process and the average cutoff temperature.

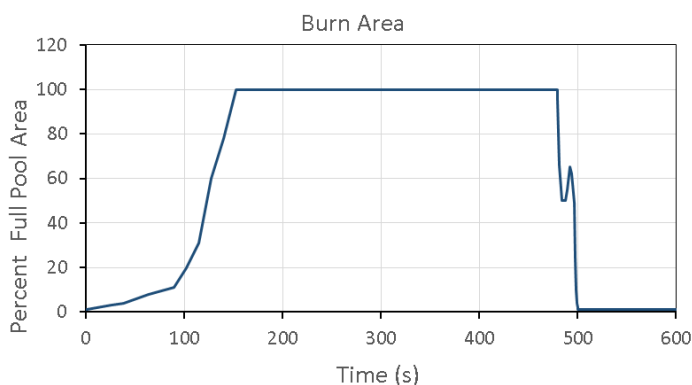


Figure 40 Burn area VIMS Rock Burn 10

The burn rates prior to boil over ranged from 0.6 mm/minute for the heavy Rock crude to 2.7 mm/minute for the light Agbami (see Table 6). Interestingly, the Agbami burned and boiled nearly continuously at a lower temperature than ANS and Rock. The fire above the Agbami slick reached only 350°C, while fire above the liquid ANS reached 450°C and the fire above the liquid Rock reached over 500°C. Agbami also had the lowest efficiency with only 66% of the oil burned relative to ANS which had the highest efficiency with 96% of the oil burning and Rock achieving a 76% burn efficiency. These differences in maximum temperature, burn rate, and efficiency are likely due to the components in the oil. These high precision high temporal measurements potentially allow the detailed study of the ISB process and the effects of the oil properties.

Table 6. The resultant burn rate and efficiency for Agbami, ANS and Rock.

Oil	Dynamic Viscosity 20°C (cP)	Classification	Environment	Burn rate before boil over (mm/min)	Burn rate during boil over (mm/min)	Thickness (mm)		Area (m ²)		Volume (L)		Efficiency
						Initial	Final	Initial	Final	Initial	Final	
ARA-VIMS												
Agbami	2	Light	Contained pool	2.7	0.3	10.7	3.6	0.5	0.5	4.9	1.6	66%
ANS	25	Medium	Contained pool	2.1	3.7	10.8	1.9	0.5	0.1	4.9	0.2	96%
Rock	2617	Heavy	Contained pool	0.6	4.0	11.2	2.7	0.5	0.5	5.1	1.2	76%

6.2. Contained burns at the indoor WPI Burn Lab

In addition to measurements outdoors at the ARA-VIMS facility multiple burns were performed indoors at the WPI burn facility. For the measurements at WPI, the thermocouples and eight transducers were mounted on a frame as shown in Figure 41. The frame was placed at the bottom of the tank with the transducers arranged circularly inside the tank. All the transducers had a center frequency of 2.25 MHz. The main difference from the ARA-VIMS burns was that this facility was indoors providing more stable temperatures and eliminating the effects of wind.

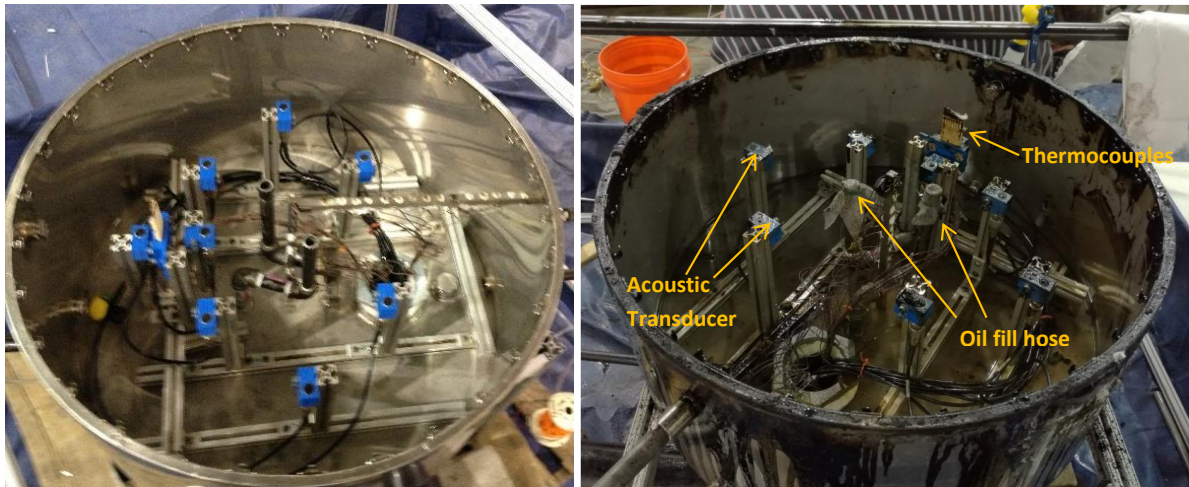


Figure 41. Acoustic transducer and thermocouples mounted inside the burn chamber before and after burning.

A series of photographs during the burning are shown in Figure 42 from the ignition through the flames burning out. The structure above the fire held thermocouples for use by WPI to measure the temperature inside the flames.



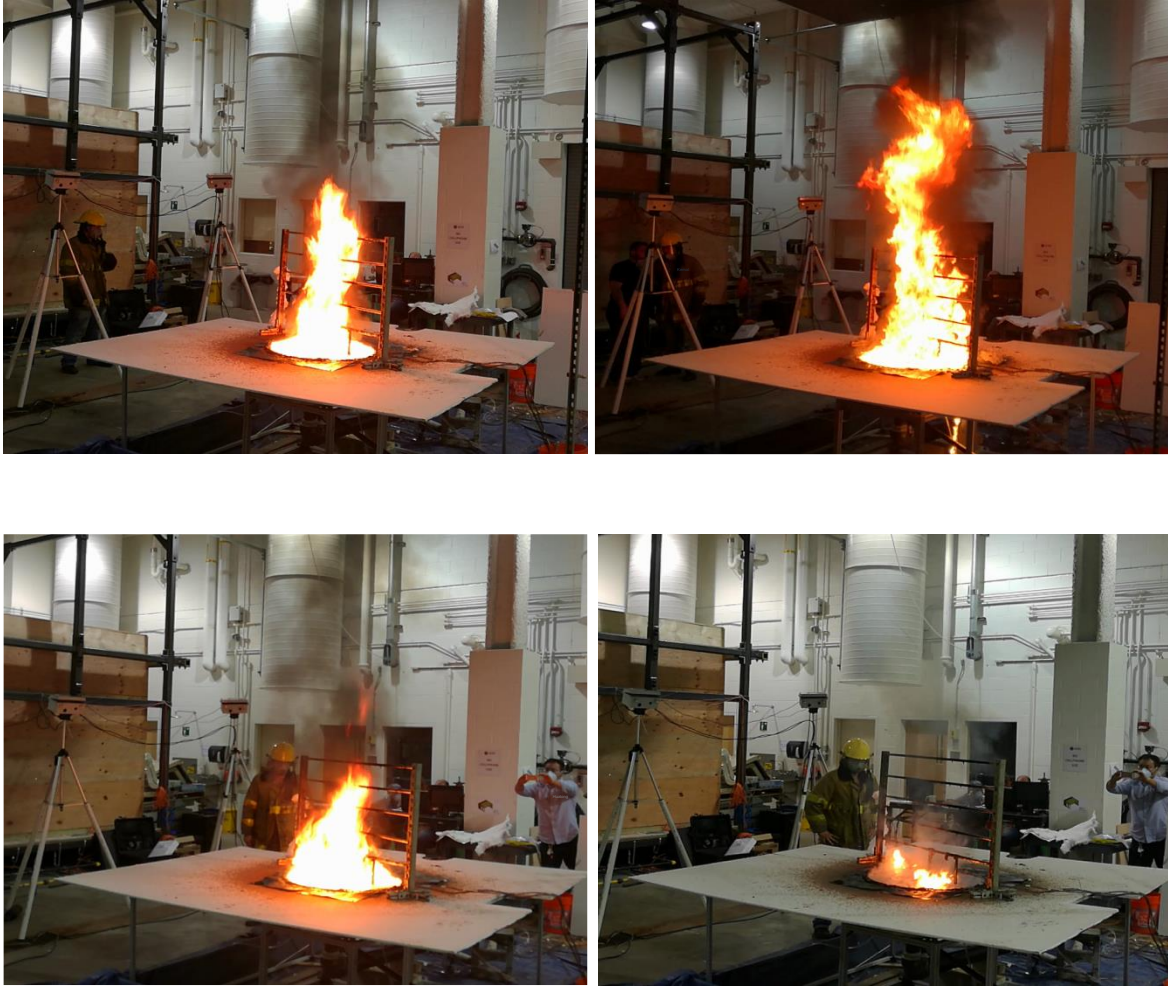


Figure 42. Photographs of several instances during burning of ANS crude oil at WPI. Top left is ignition and bottom right is just before the flames died out.

The thickness for the burns at WPI was calculated assuming the average cutoff temperature derived from the validation process for two burns. The temperature, acoustic signal and thickness are shown in Figure 43 and Figure 45.

WPI Burn 5 ANS

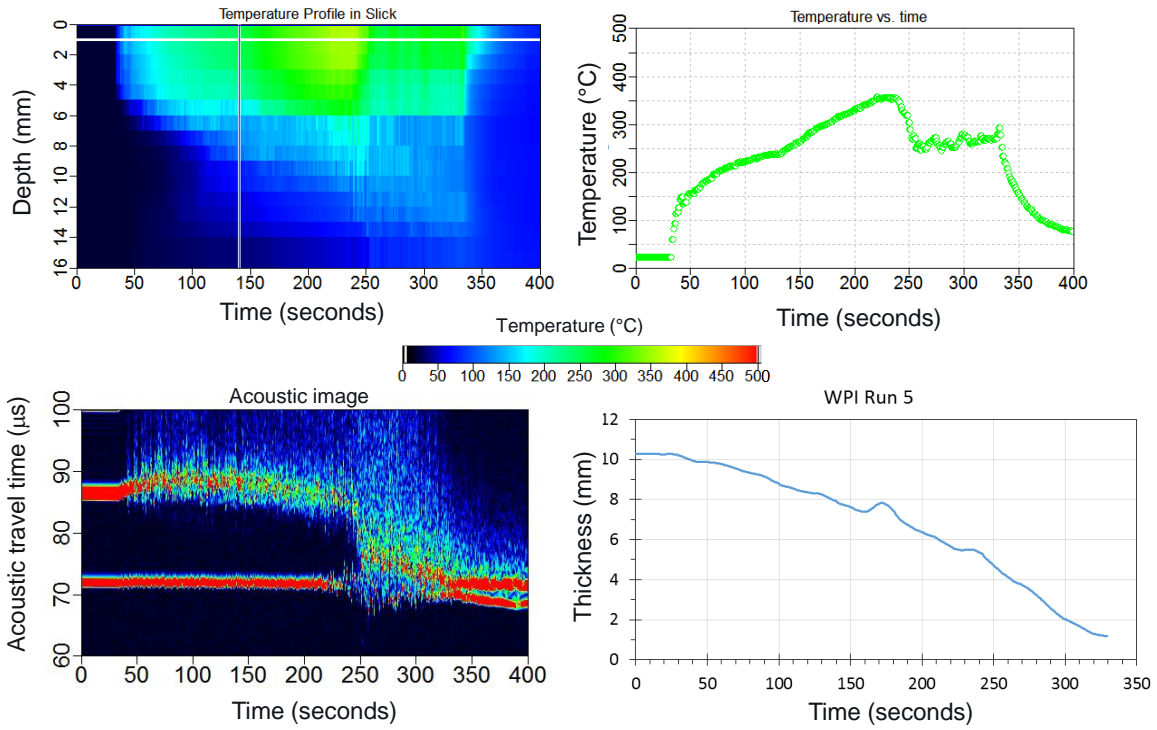


Figure 43. The temperature profile, acoustic image, and resultant thickness for ANS burn 5 using the average cutoff temperature.

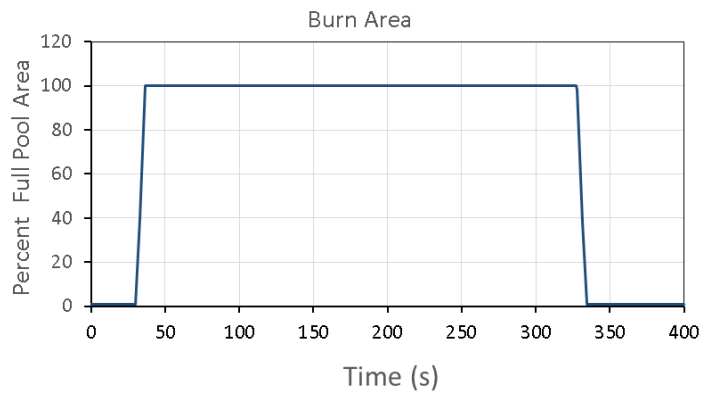


Figure 44. Burn area WPI Burn 5

WPI Burn 6 ANS

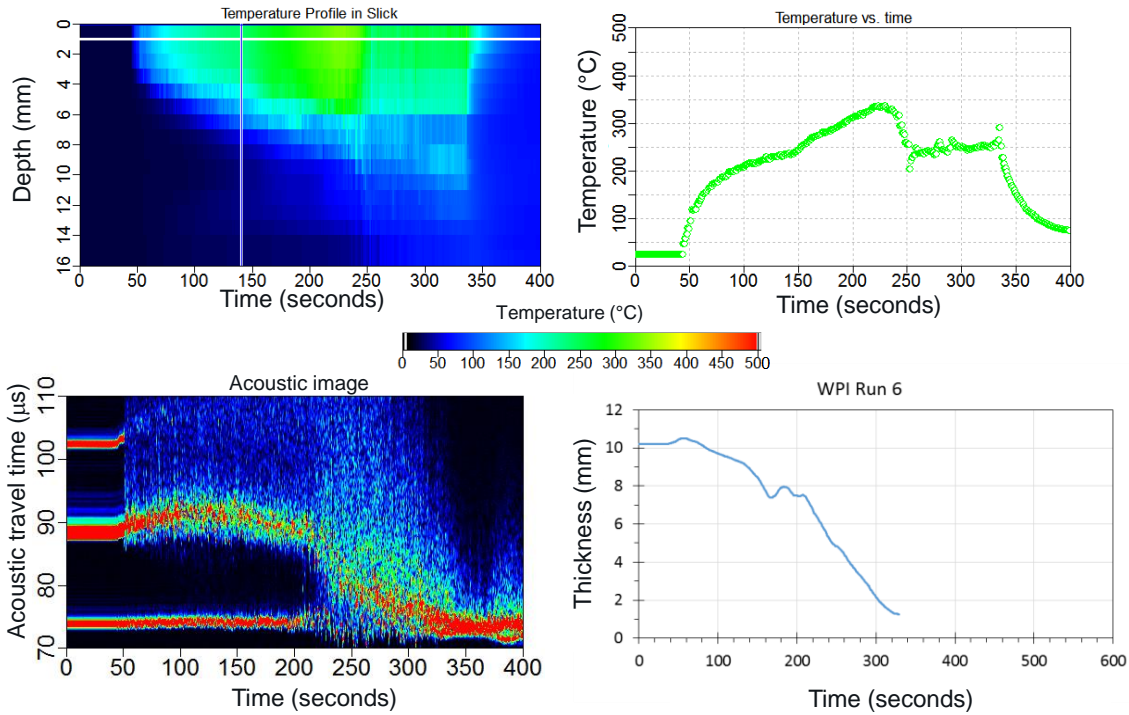


Figure 45. The temperature profile, acoustic image, and resultant thickness for ANS burn 6 using the average cutoff temperature.

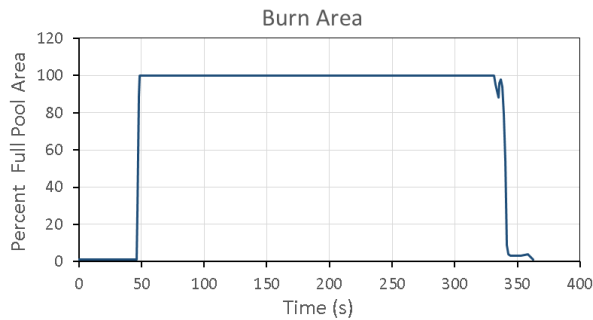


Figure 46. Burn area WPI Burn 6

The burn rates and efficiency for these burns at WPI (see Table 7) was very consistent likely due to the internal controlled atmosphere compared to the outdoor ARA-VIMS burn facility. The burn rates and efficiency were lower than the ANS at the outdoor ARA-VIMS facility, with an efficiency of 87% relative to 96% at the outdoor ARA-VIMS facility.

Table 7. The burn rate and efficiency for ANS at WPI

Oil	Dynamic Viscosity 20°C (cP)	Classification	Environment	Burn rate before boil over (mm/min)	Burn rate during boil over (mm/min)	Thickness (mm)		Area (m ²)		Volume (L)		Efficiency
						Initial	Final	Initial	Final	Initial	Final	
WPI												
ANS Burn 5	25	Medium	Contained pool	1.5	3.0	10.3	1.3	0.4	0.4	3.9	0.5	87%
ANS Burn 6	25	Medium	Contained pool	1.4	3.2	10.2	1.4	0.4	0.4	3.9	0.5	87%

6.2.1. Area calculations of small contained burns

At WPI the area computation was performed live with all six visible light cameras. Imagery from all six cameras were saved to disk every 2 seconds and as an intermediate step in the area computation rectified images from all six cameras were also saved. The six rectified images were overlaid and processed to determine area. Some examples of the burning oil images are shown in Figure 47. Four images for each of the six visible light cameras are shown on the left and the four respective rectified images are shown on the right.

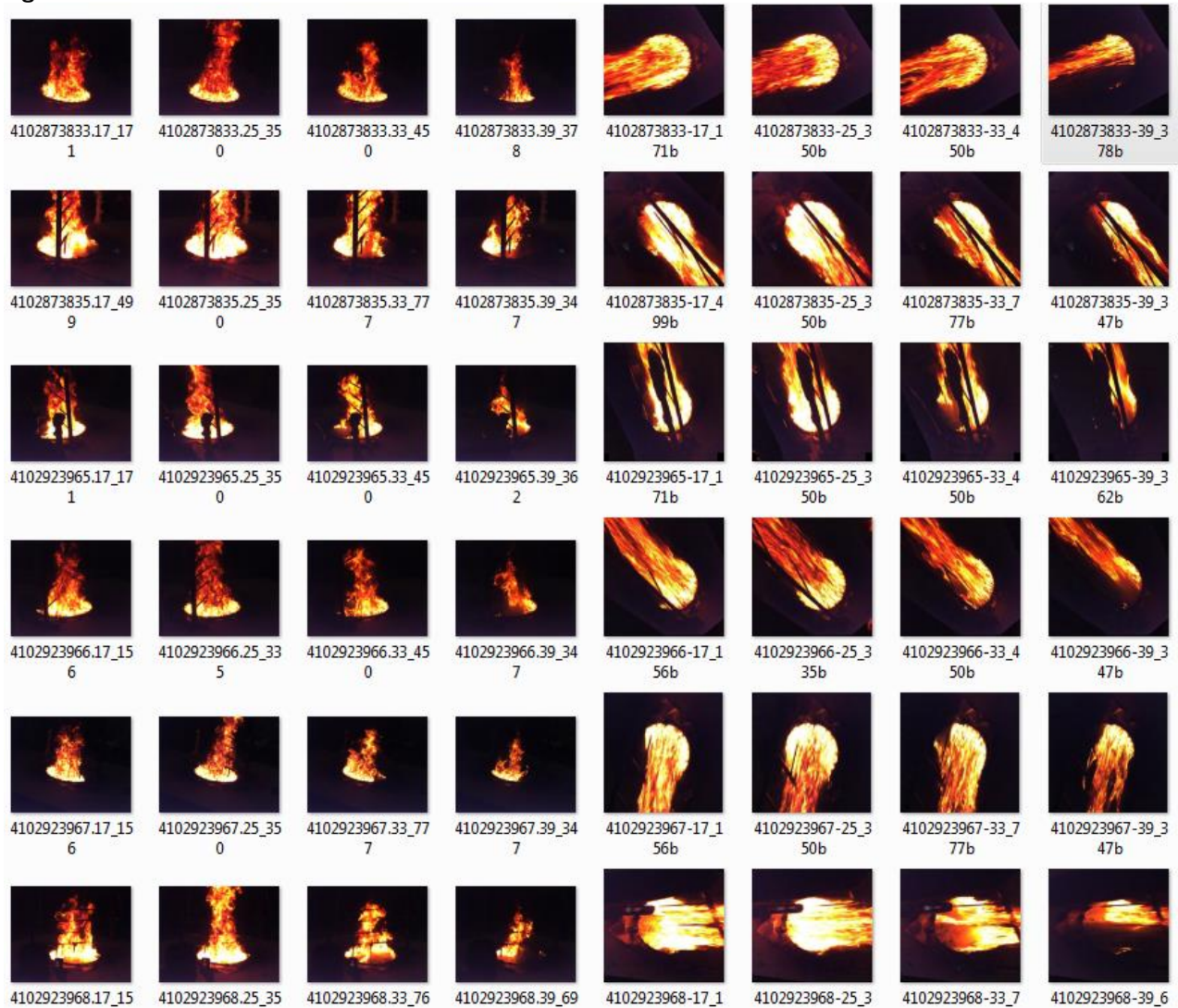


Figure 47. ANS ISB at WPI: Original imagery left, rectified imagery right

One outcome of the experiments was to determine the effect of permanent blockage on the final area. Shown in Figure 48 are metal bars with thermocouples which were placed above the fire during the burns to measure temperature. These bars were projected on the rectified area images and funneled down in to the final area determination. Since the algorithm summed non-burning areas, a bar appearing in any

images was counted as a non-burning region. The silhouette of the bars can be seen in both Figure 47 and Figure 49. The final area shown in the bottom row of Figure 49 shows the effect of the bars have on the area.



Figure 48. Image of the ISB with the instrumentation bars in the flames.

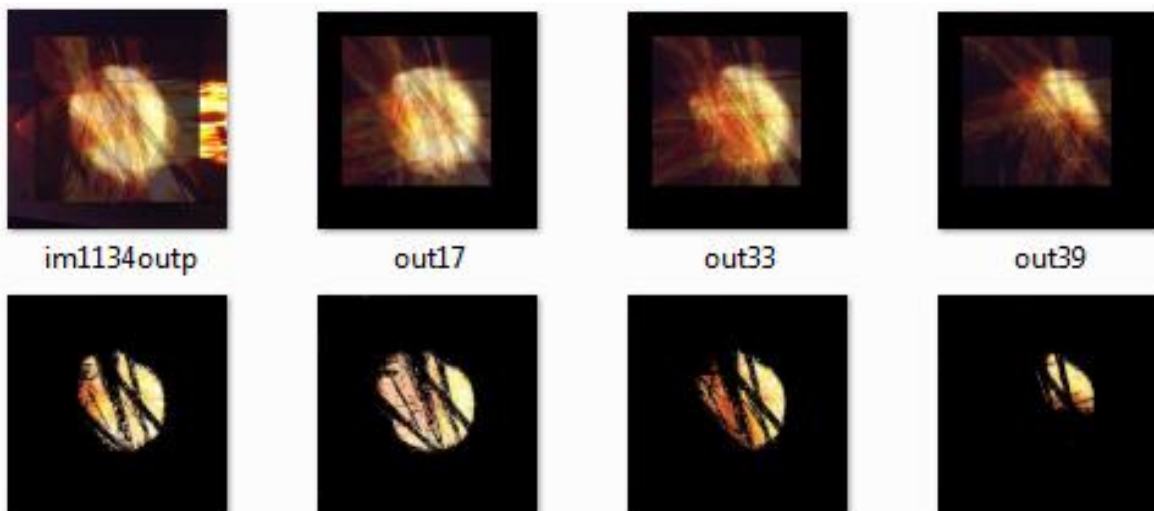


Figure 49. Overlay of all views top, bottom is area computed

6.3. ISB of oil in small cavities of ice

We performed multiple burns in ice fields at the Geophysical Research Facility (GRF) at the Cold Region Research and Engineering Lab (CRREL), a 60-foot long x 22-foot wide x 7-foot deep concrete basin. During these burns, the surface of the water was covered with ~22 inches of ice. An aerial photograph of the tank is shown in Figure 50. Photographs of the test area with the ice cover are shown in Figure 51 and Figure 52.



Figure 50. The Geophysical Research Facility (GRF) facility at CRREL in the purple box.



Figure 51. The GRF site covered with ice. The electronics were set up under the blue tarp.



Figure 52. The GRF showing retractable roof, pristine ice and our instrumentation canopy before testing.

To install our acoustic equipment below the water, a hole was cut in the ice. The cameras were installed on tripods at various locations around the hole as shown in Figure 53. The acoustic equipment and thermocouple tree were installed on a platform below the water surface as shown in Figure 54.



Figure 53. White camera enclosures on tripods prior to testing at the CRREL ice facility. The frame to hold the transducers is behind the blue board.

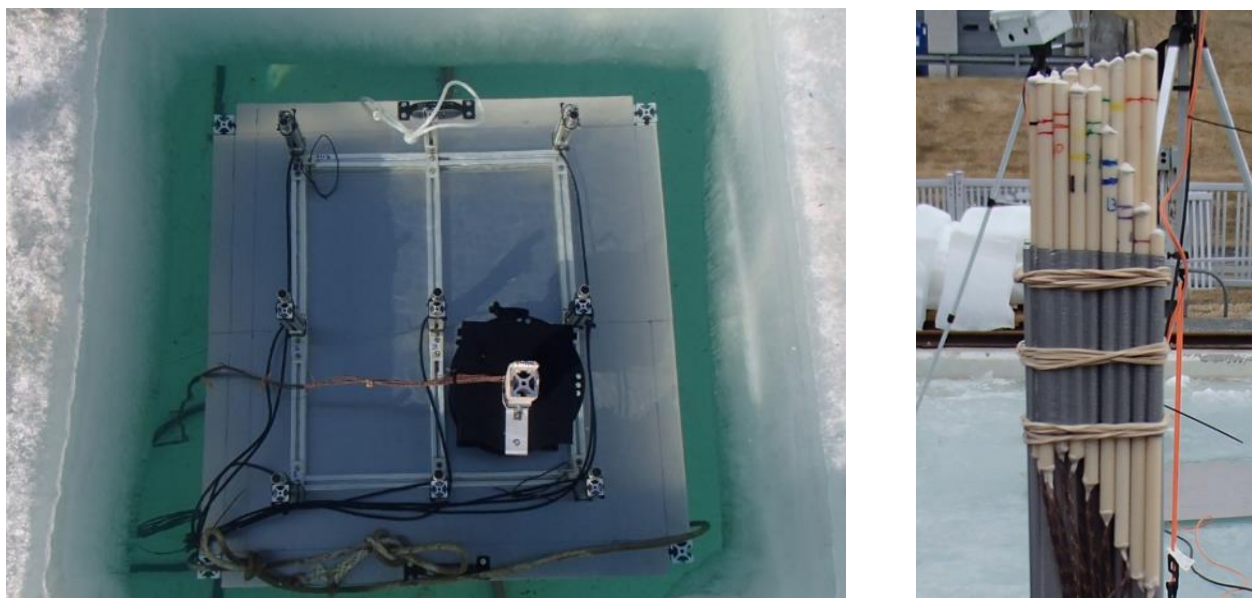


Figure 54. Transducers and thermocouple tree mounted on frame under water. The right photograph shows the thermocouple tree prior to burning.

Figure 55 shows the set up after several burns opened up a large area of open water. As part of these measurements, we also deployed our acoustic sensors on a free-swimming ROV with will be discussed in a separate section.



Figure 55. Large opening in ice for measurements in ice fields.

6.3.1. Area measurement of ISB in ice fields

At CRREL the area computation was performed automatically using multiple cameras at about 1 frame per second. The images from the burns were archived in video format for study and identify error cases in order to improve the algorithm. The images were analyzed and run through processing code multiple times since in order to improve the area algorithm. Figure 56 shows the progression as three images were used to compute burn area. The top row are the original images. The second row were transformed to top down view and the single image at the bottom is a composite created by placing the detected fire area in the Red, Green, and Blue channels. The intersection of the fire is the white area which is an estimate of the fire on the surface of the water.

The artifact of coloring each camera R, G and B is the intersection of camera pairs take on a mixture color. So the intersection of cameras 1&2 is pink, cameras 1&3 is yellow, and 2&3 is teal.

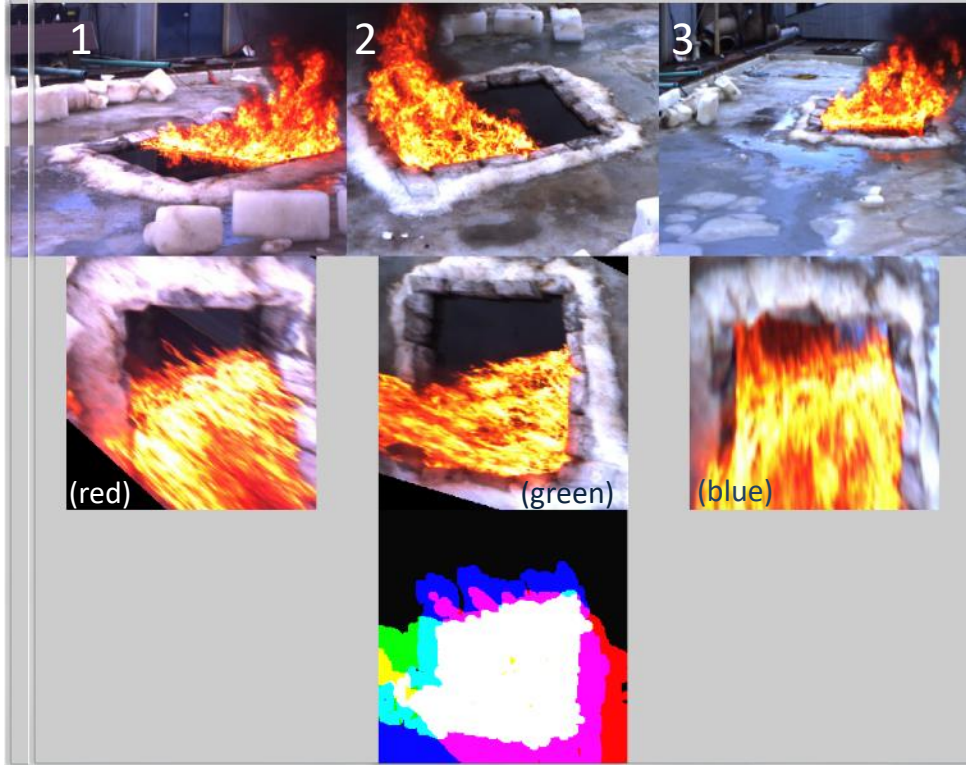


Figure 56. Three images used to compute burn area. The bottom image shows the overlap of the three images with the white region estimating the burn area on the surface of the water.

The snow piled up in front of image 3 occluded a portion of the water surface. In the rectified image, the snow ridge looked like it over-hangs the water at the top of the image, this artificial overhang is a distortion created by the rectification process. Figure 57 shows how the snow obscures the water surface from view. Open water will typically not have such persistent obstructions.

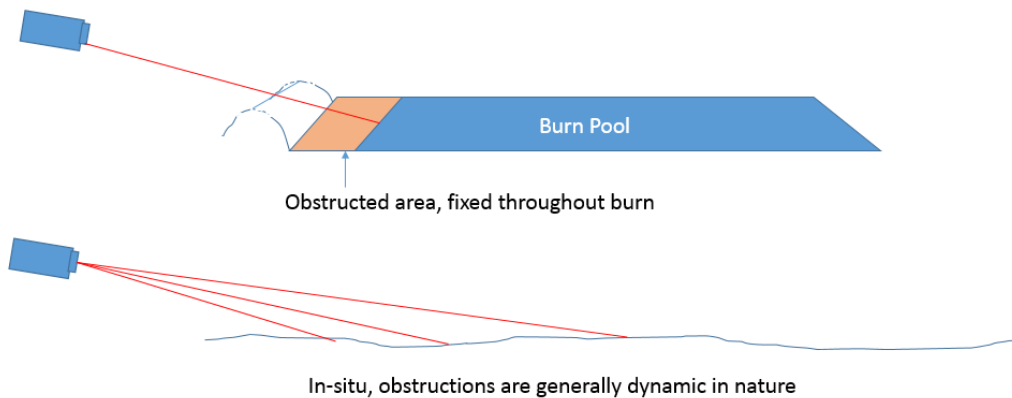


Figure 57. The pink area shows the part of the water surface obscured by the snow on the side. Some key take-aways from the image analysis for ISB at CRREL are:

Low Camera Angles: The placement of cameras at low angles stressed the algorithm due to the difficulty of registration to the birds eye view because the pixels were more stretched out and the transform needed to be more mathematically precise to rotate the image from a 20 degree vantage point to simulate a 90 degree (normal) vantage point. The camera height of the plane of the fire to distance away from the fire ratio determines the difficulty in using automated procedures to transform the image so it is usable in the overlay. We used a wide range of cameras settings in this study and can use the results from over 30 burns to empirically determine error and verify the limits of forming an accurate homography.

Distant Cameras: The area computation does not require a large number of pixels on target. The data suggests 150 x 150 pixels over the fire area can supply the same accuracy as images with five times as many pixels. The difficulties in fire edge classification and obstruction due to smoke or objects has a larger effect than distant camera setting or lower resolution cameras. We have used 900 x 700 pixels on the fire and as low as 200 x 100 pixels from the recent CRREL burns where we placed cameras further away on the movable gantry.

Smoke, Reflection: There are several features that can affect the accuracy of an image based classification process including reflections of fire from the water surface and obstructions of the fire. We overcame these issues predominantly by using images from multiple cameras. Specifically, for any image based classifier it is almost impossible to distinguish fire from a reflection of fire for both IR and for visible cameras. We eliminate the reflection by intersecting the images seen from many rectified cameras. Shown in Figure 58 is an example of the multiple camera configuration ignoring the reflection from the water recorded on the rightmost camera.

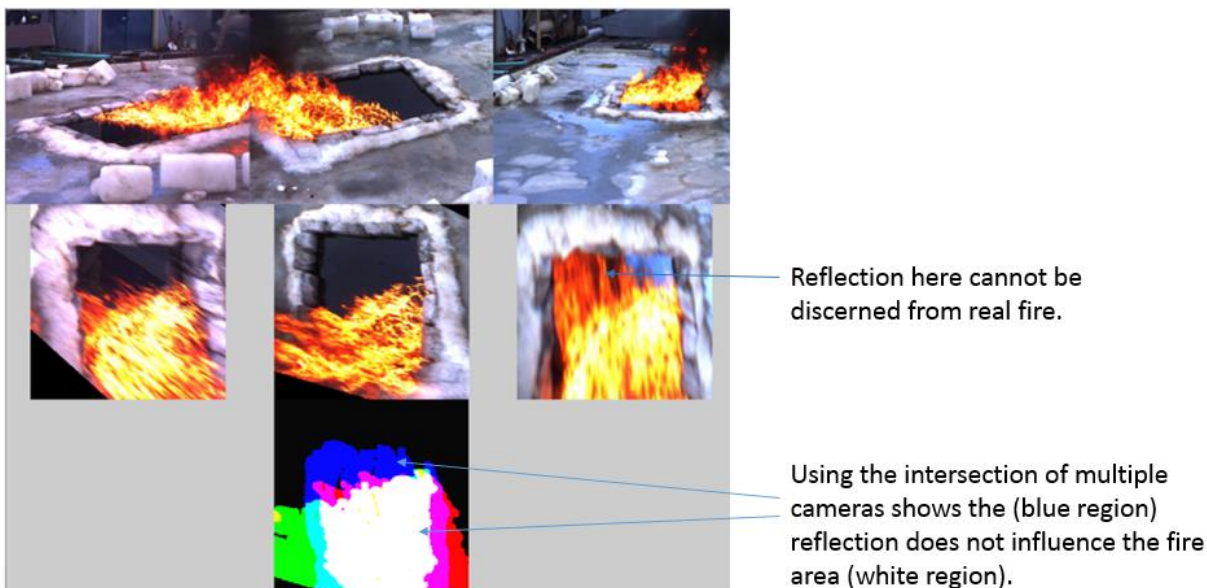


Figure 58. Multiple cameras are combined to eliminate reflection off the water in one of the images (right).

As mentioned previously, obstruction creates an issue for the algorithm. If the obstruction can be detected, the camera with the obstructed view can be eliminated from the calculation. In Figure 59 heavy smoke obscures the fire.

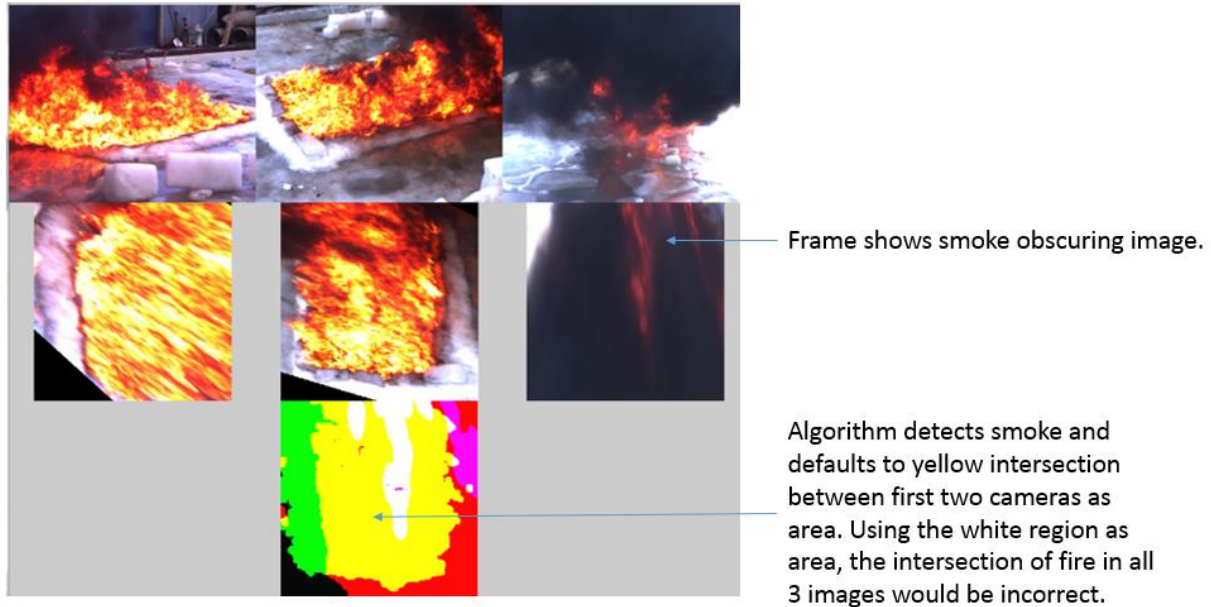


Figure 59. Due to smoke in one image the intersection of the fire results in an incorrect area (white). By eliminating the image from the image pool the intersecting region defaults to the yellow.

The process identifies the obstructing smoke by noting the overall fire coverage is less than 60% of the coverage in the other images and then drops the frame dynamically. This method is a very simple and we are experimenting with more sophisticated smoke detection such as implementing a frame by frame differencing.



Figure 60. IR image shows reflection and smoke. The fire and smoke blend together because they both go over the upper threshold for the uncooled long wave IR.

Smoke and reflections are also issues with the longwave IR camera. The smoke is indistinguishable from the fire as it contains heat. So instead of a negative obstruction it creates a larger false positive for fire which can lead to overestimation of fire. With enough cameras false positives can also be eliminated. The area algorithm itself works well for 3 or more cameras. Two cameras can be used but they need to be near 180 degrees, (opposite ends of the fire) and free of obstructions including smoke.

The ISB measurements at CRREL provided images from a significantly more expensive mid-wave IR camera shown in Figure 61. The higher range allowed us to see the difference in temperature between smoke, fire off the surface, and fire near the surface of the water. The question that arises: Is it possible that a more accurate oil combustion rate could be computed from the volume of hot fire and the surface area of the burn together than just from the surface area alone?

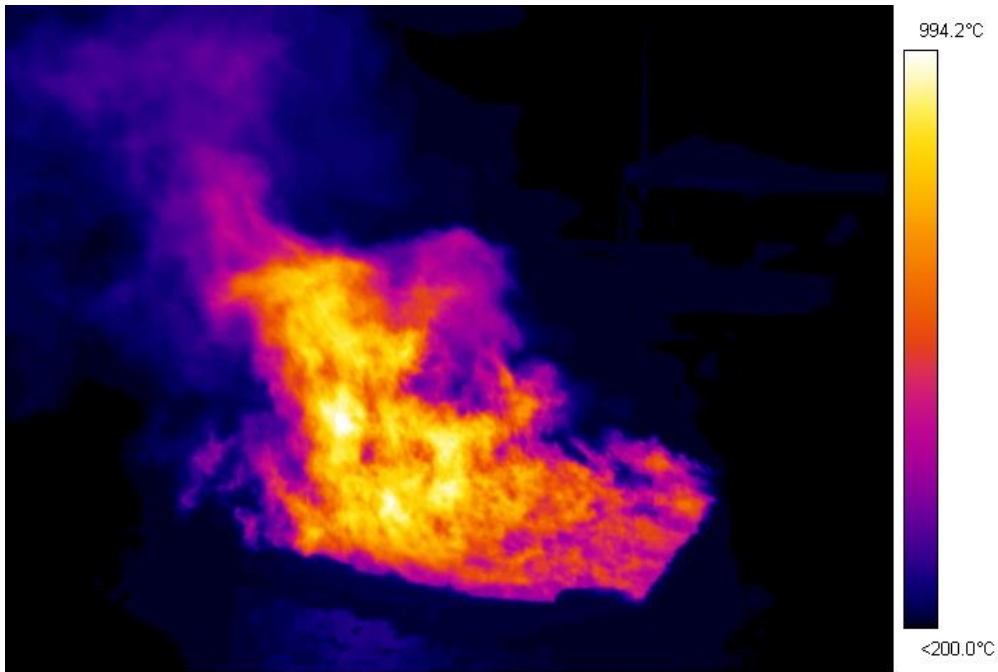


Figure 61. The mid wave IR camera image. It has a higher upper range and better resolution of the temperature in the fire.

The area of the burning oil for the three burns of ANS at CRREL are shown in Figure 62 and one particular burn in Figure 63. The identification of fire and extraction of the area was automated from start to finish and operated on streaming video.

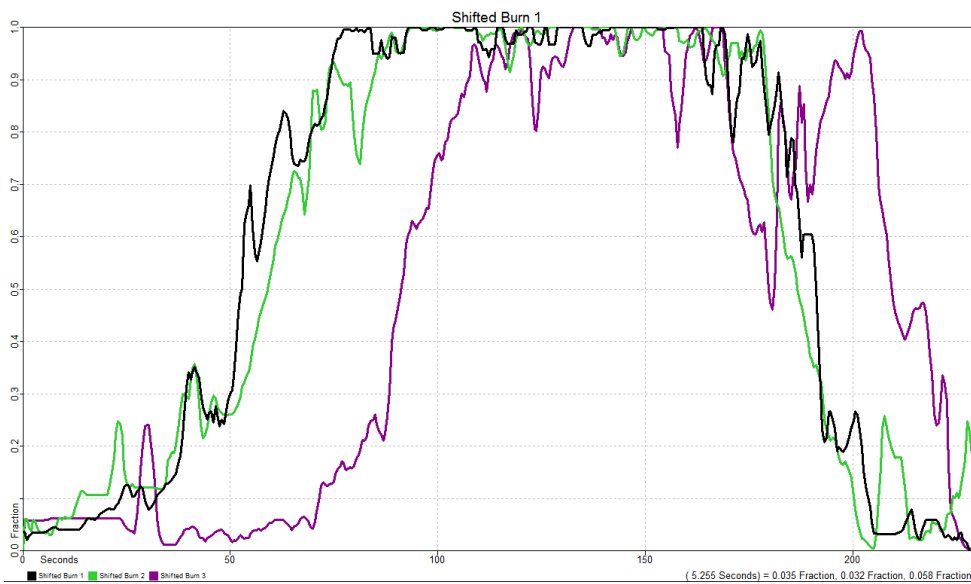


Figure 62. The surface area of the burning oil for multiple ANS burns from a completely automated process.

The only part of the process that was not automated at CRREL is the determination of the homography matrix for each image. This matrix is a key element for deployment of the technology and is the next functional upgrade of the algorithm.

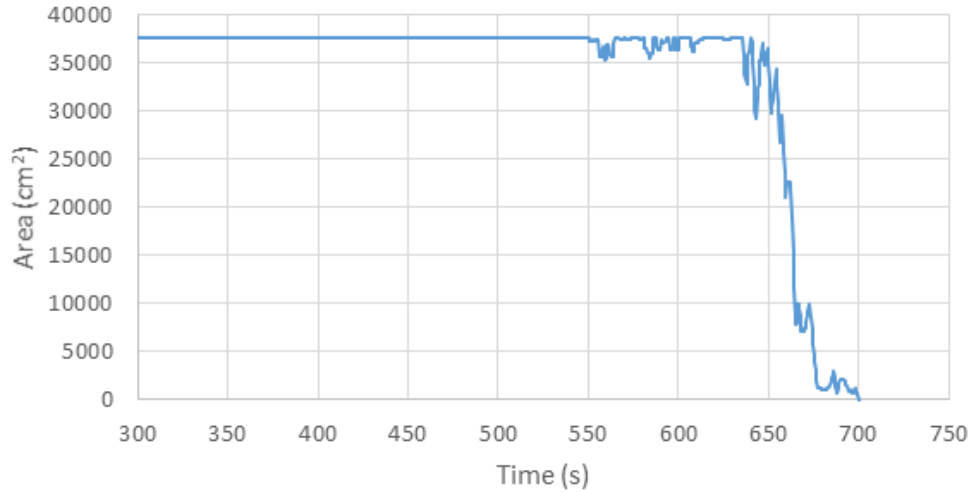


Figure 63. The fractional area of the ANS oil covering the water for burn 7.

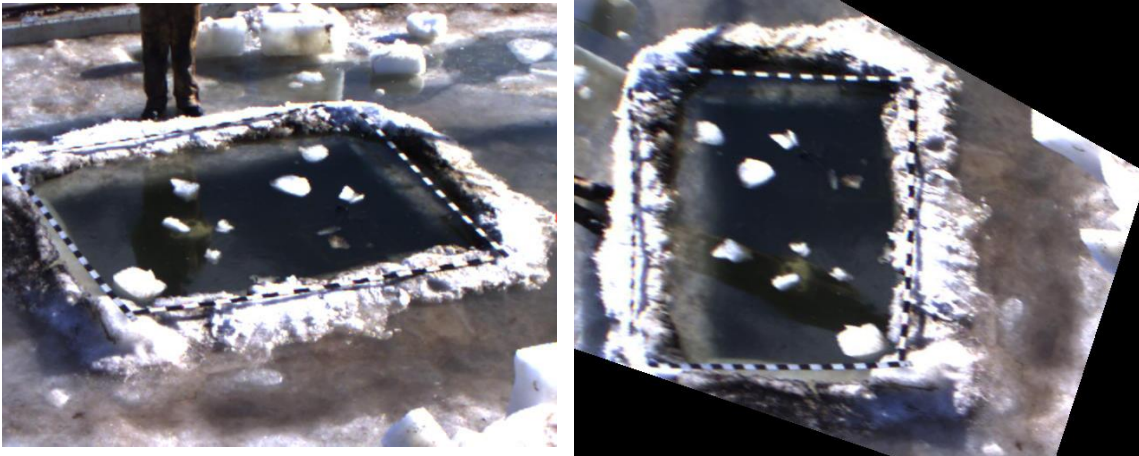


Figure 64. Left, original image. Right, area preserving planar homography.

Homographic re-projection of a plane in an image is very well established method for transforming all the patterns belonging to that plane while preserving the geometric relationships in the would be 3D projection that image. By projecting the plane (the surface of the water) so it physical coordinates align with that of the image pixel coordinates we can use a simple scaling factor to convert pixels to distances. The conversion works in both X and Y directions as shown in Figure 65.

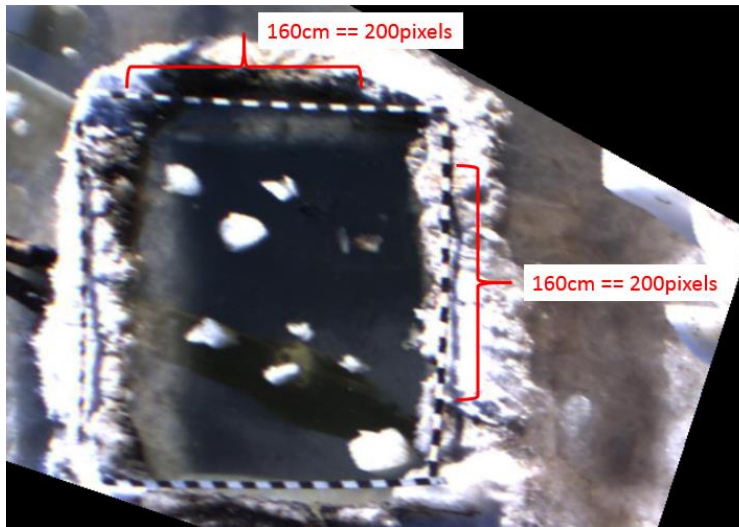


Figure 65. Pixel to cm conversion factor validated by placing rulers in field

For Burn 9, the conversion from pixels to cm is 0.8cm / pixel for the projection shown. The rulers used to validate the conversion are slightly off the plane of the water so will show some bending. The ideal way to calibrate a conversion is to use objects of known dimensions floating on the water surface.

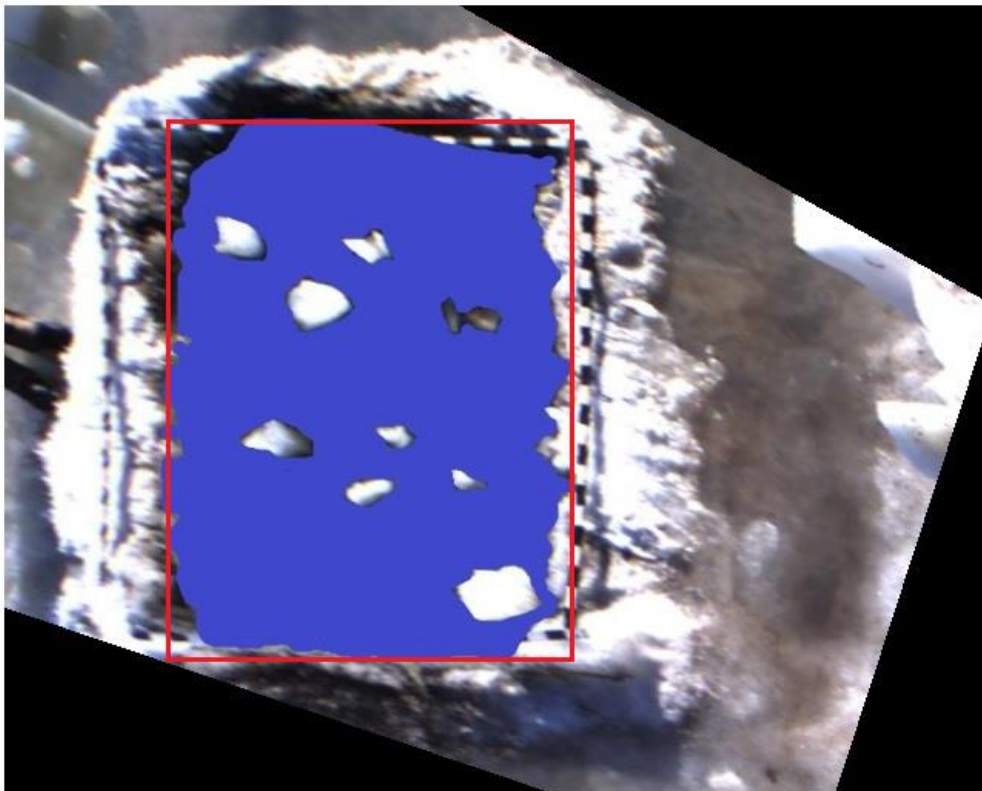


Figure 66. Water surface colored blue, the red square is the very reasonable human measurement which came out to estimate the surface area as 58800cm²

The actual water surface area was colored blue. An automatic summing routine found 72249 pixels match the monochromatic unique coloring of the water surface area. This translates to an actual surface area as follows:

$$72249 \text{ pixel}^2 * .8 \text{ cm/pixel} * .8 \text{ cm/pixel} = 46239 \text{ cm}^2$$

The measurement made on site based on a tape measure in both directions of 210cm x 280cm shown as the red rectangle in Figure 66 was 58800 cm². All the CRREL burn basins were measured from the largest horizontal and vertical dimension touching water and the product was used as the area estimate. For all the CRREL burns, the area computed with image processing vs. the area estimated from a rectangle.

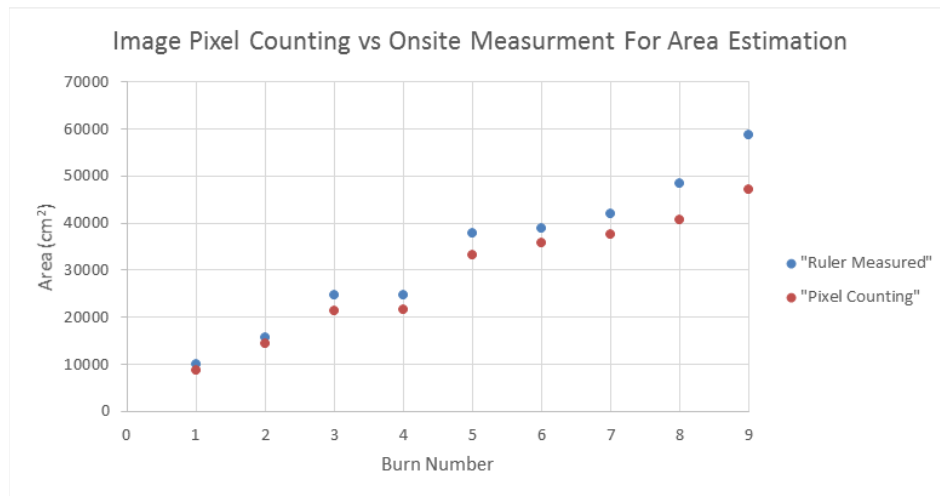


Figure 67. Area for January 2017 CRREL burns

The CRREL burns all occurred in the same ice cut out and were occasionally rebuilt with ice, but generally got larger as the testing continued. The rectangle measured to the largest hole dimension in both x- y direction consistently yielded a larger estimated area at the start of the burn. The first two area estimates were similar as the hole was freshly cut and closer to a rectangle. There was also no ice set out to float in the first smaller burns.

6.3.2. Acoustic measurement of thickness for ISB of ANS oil in ice fields

To further test the ability to measure the slick thickness in more realistic environments, the thickness of a burning pool of oil in an ice cavity was calculated using the same cutoff temperature derived previously for ANS at our ARA-VIMS burn facility. The resultant data are shown in Figure 68. These burns were fundamentally different than burns in water with no ice. First, the acoustic image in the bottom left figure shows the bottom of the slick rising as the burn progressed. The rise is caused by melting ice increasing the water level. While it was simple to calculate the travel time through the slick, determining the temperature in the slick was not simple because the oil rose above the thermocouples. The resultant temperature profile shows the maximum measured temperature achieved was ~150°C indicating the top thermocouple remained in the oil or in the water below the

oil throughout the burning process. For completeness the thickness, burn rate, and efficiency are is calculated.

CRREL March 2016: Burn 2

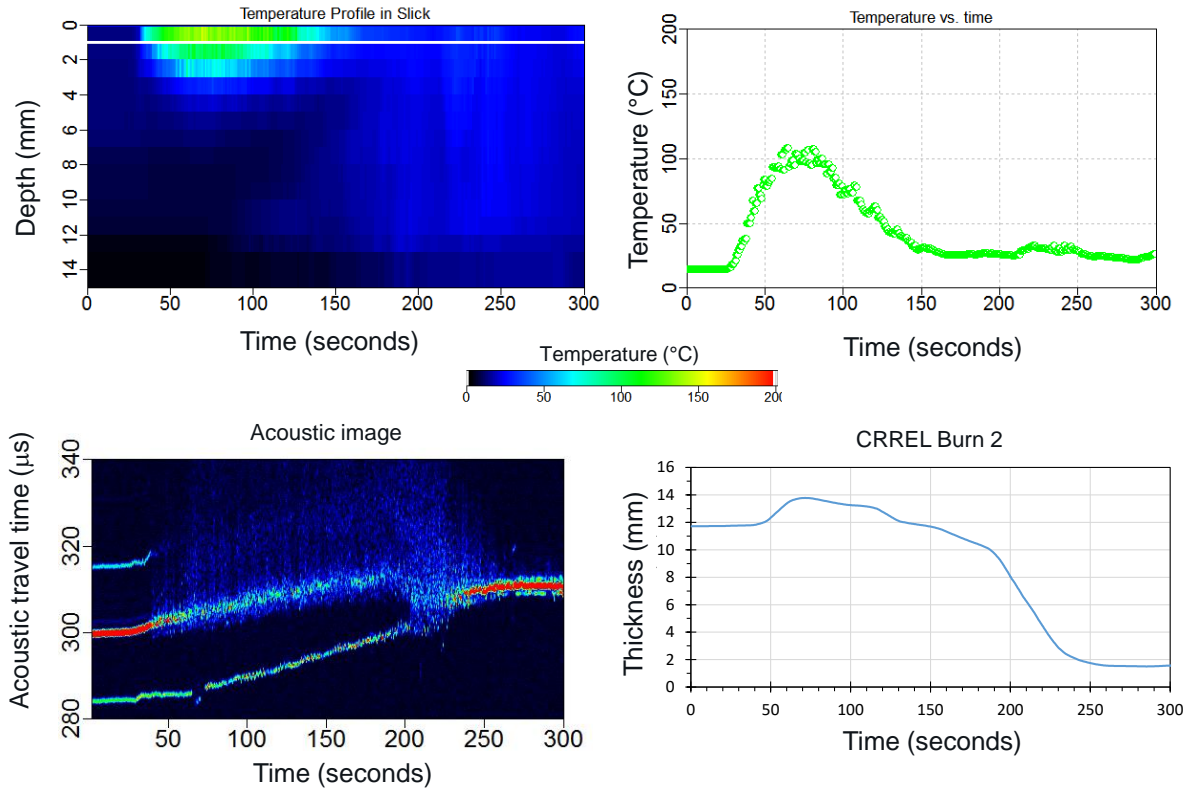


Figure 68. The temperature profile, acoustic image, and resultant thickness for ANS in an ice cavity using the average cutoff temperature

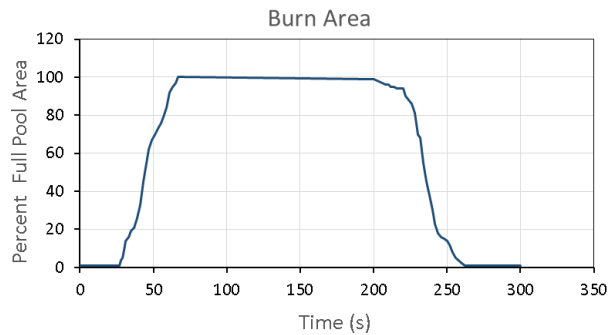


Figure 69. Burn 2 area computation

The Area computation for burn 2 shows the burn progressed to 100% in 15-20 seconds and burned over the entire opening for over 150 seconds before receding. Figure 70 shows a more interesting burning situation where an enlarged hole was filled with oil and ice. During burning the slick did not burn uniformly as shown in Figure 70, Figure 71, and Figure 72. The resultant temperature profile and acoustic measurements are shown in Figure 73.



Figure 70. Prior to burning



Figure 71. During burning with nearly full coverage



Figure 72. During burning with partial coverage

CRREL March 2016: Big Byrne 5

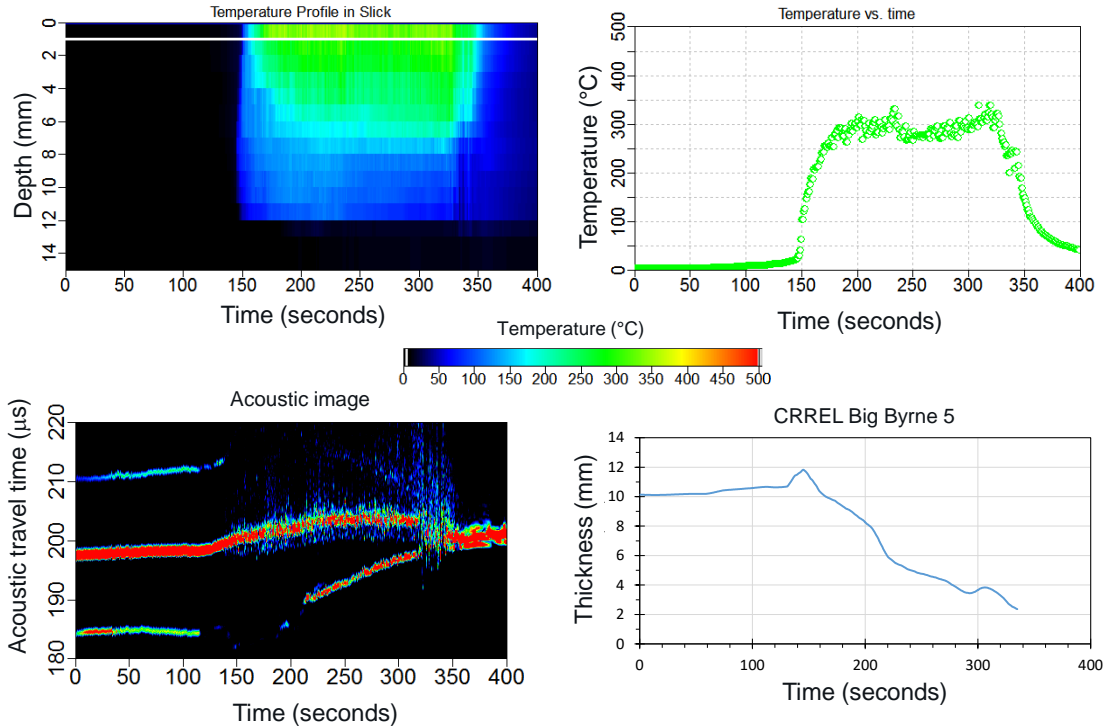


Figure 73. The temperature profile, acoustic image, and resultant thickness for ANS in an ice field using the average cutoff temperature.

For this set of measurements the thermocouples were placed lower so that they remained covered during the burning resulting in a temperature profile that is more similar to other burns. The thickness has a complex shape and may be related to the inhomogeneous burning and an inhomogeneous thickness of oil across the ice cavity as demonstrated by the area computation Figure 74.

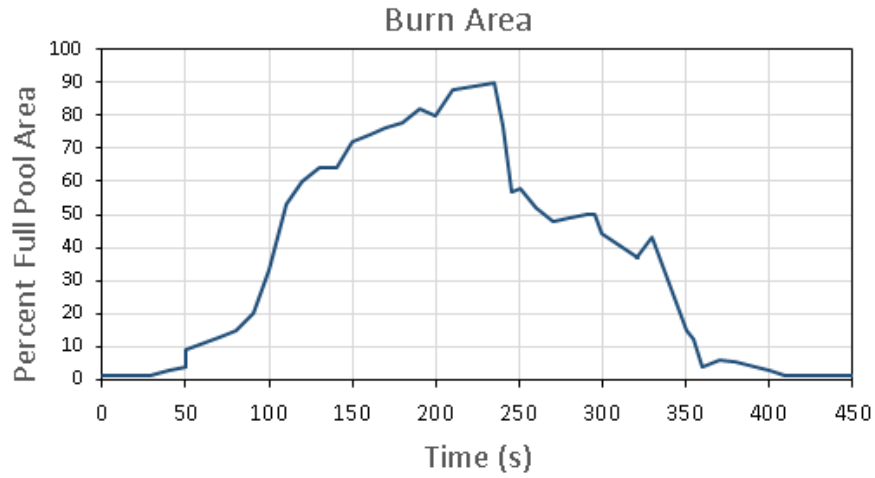


Figure 74. Big burn area computation.

The remaining three burns at CRREL were also complex due to the presence of ice, the cold water, and the melting of ice during the burn. The results are shown in Figure 75, Figure 77, and Figure 79.

CRREL January 2017: Burn 2

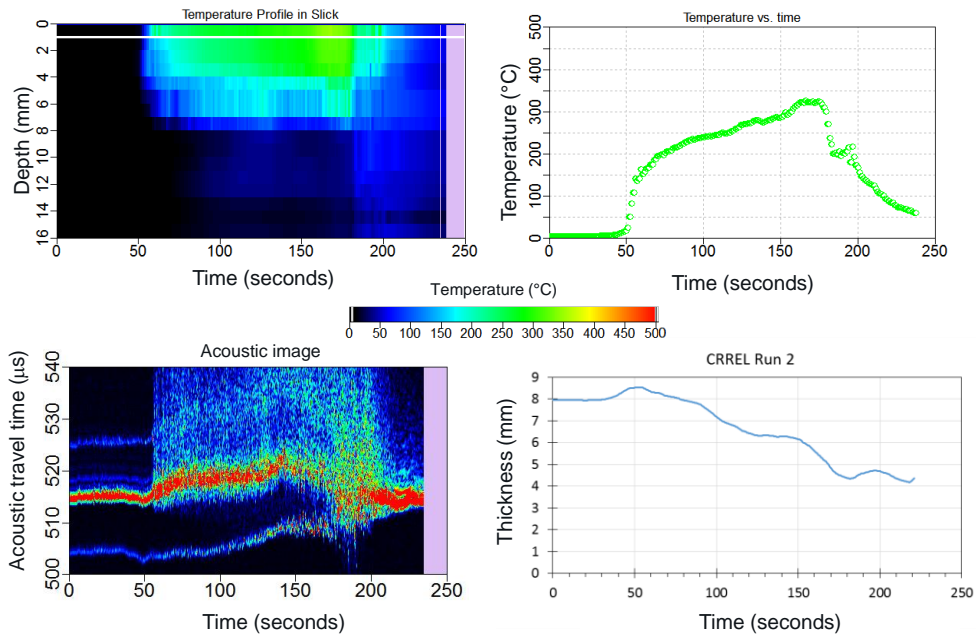


Figure 75. The temperature profile, acoustic image, and resultant thickness for ANS Burn 2 in an ice cavity using the average cutoff temperature.

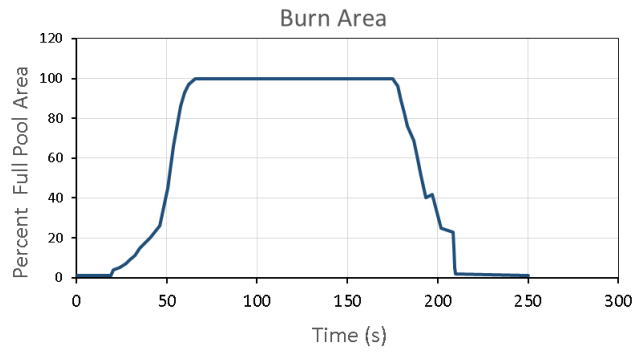


Figure 76. Burn area ANS Burn 2

CRREL January 2017: Burn 7

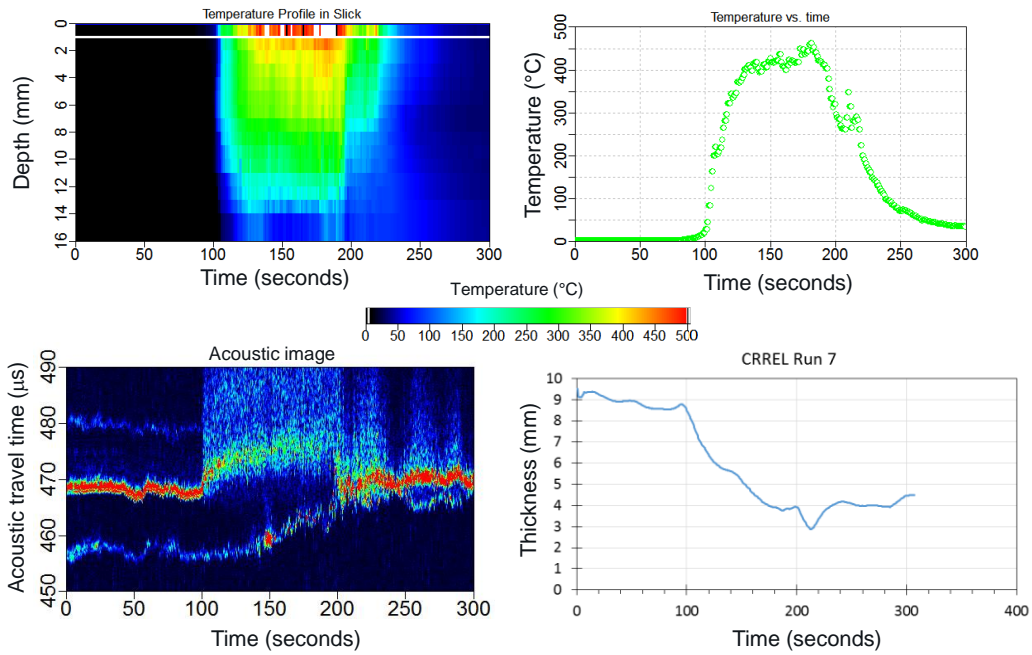


Figure 77. The temperature profile, acoustic image, and resultant thickness for ANS Burn 7 in an ice cavity using the average cutoff temperature.

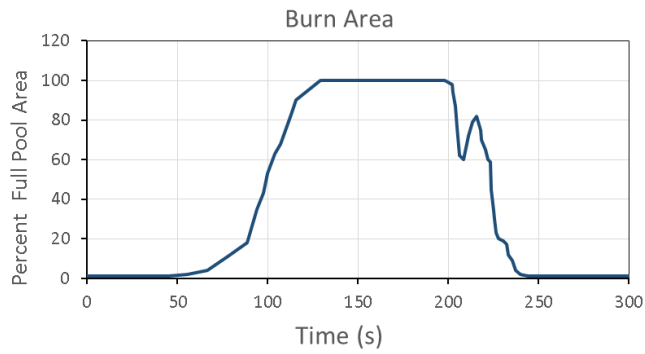


Figure 78. Burn area ANS Burn 7

CRREL January 2017: Burn 9

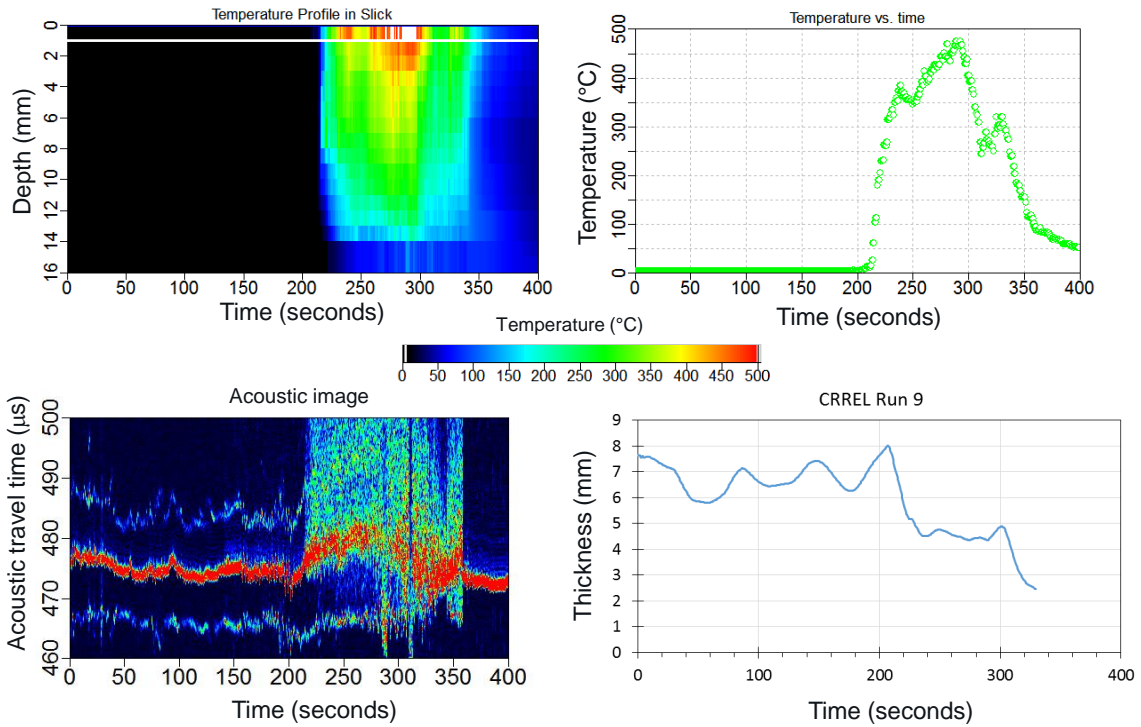


Figure 79. The temperature profile, acoustic image, and resultant thickness for ANS Burn 9 in an ice cavity using the average cutoff temperature.

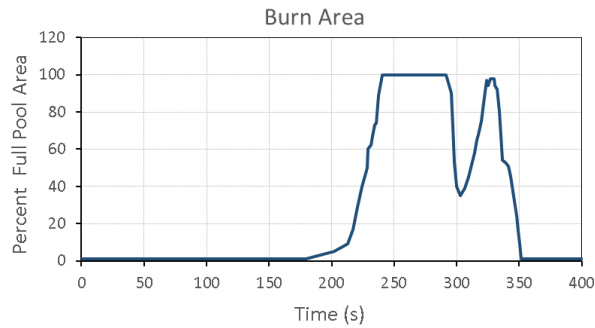


Figure 80. Area for ANS Burn 9 at CRREL.

The resultant burn rates and efficiency of these burns at CRREL along with all of the burns are shown in Table 8. With the exception of the first burn at CRREL, those burns had the lowest efficiency. This first burn at CRREL may be an anomaly because of the use of temperature data from submerged thermocouples. The lower efficiency in the other burns at CRREL is likely due to the colder water and the presence of ice in some burns. Overall the procedure to calculate the thickness, burn rate, and efficiency were robust.

Table 8. Measured burn rates and efficiencies.

Oil	Dynamic Viscosity 20°C (cP)	Classification	Environment	Burn rate before boil over (mm/min)	Burn rate during boil over (mm/min)	Thickness (mm)		Area (m ²)		Volume (L)		Efficiency
						Initial	Final	Initial	Final	Initial	Final	
ARA-VIMS												
Agbami	2	Light	Contained pool	2.7	0.3	10.7	3.6	0.5	0.5	4.9	1.6	66%
ANS	25	Medium	Contained pool	2.1	3.7	10.8	1.9	0.5	0.1	4.9	0.2	96%
Rock	2617	Heavy	Contained pool	0.6	4.0	11.2	2.7	0.5	0.5	5.1	1.2	76%
WPI												
ANS Burn 5	25	Medium	Contained pool	1.5	3.0	10.3	1.3	0.4	0.4	3.9	0.5	87%
ANS Burn 6	25	Medium	Contained pool	1.4	3.2	10.2	1.4	0.4	0.4	3.9	0.5	87%
CRREL												
ANS Burn 2, 2016	25	Medium	Ice cavity	2.0	9.5	11.7	1.5	1.0	1.0	11.7	1.5	87%
ANS Big Burn 5	25	Medium	Large ice field	2.6	5.1	10.1	3.3					
ANS Burn 2, 2017	25	Medium	Ice cavity	1.8	0.3	7.9	4.2	2.1	1.7	17.0	7.1	58%
ANS Burn 7	25	Medium	Ice cavity	2.6	0.6	9.4	4.0	2.9	2.8	27.1	11.0	59%
ANS Burn 9	25	Medium	Ice cavity	7.5	0.2	7.4	2.8	5.3	1.0	39.2	2.7	93%

7. Transitioning Towards Operational Environments

While we have made great advancements to develop a functional measurement of the instantaneous thickness, area, burn rate of oil, and burn efficiency there are many engineering challenges for deploying these measurements in open water for a real ISB event. One potential option for field use is to provide instantaneous burn rate and thickness measurements to the boat operators so that their speed can be adjusted to collect more or less oil in the boom to maintain maximum burn rate at the optimum thickness for the duration of the burn. In addition, these continuous measurements of burn rate will provide accurate inputs into the oil balance calculations. The specific challenges that we see at this time are described below.

7.1. Surface area measurements

There are several obstructions that could be present in an operational environment such as wind-driven smoke that, if dark enough, can be classified as a non-burning area. To overcome these obstructions, it is likely that performing temporal and spatial measures of fire area for each camera will remove these artifacts. A blockage moving across a scene will have a pattern in successive frames and, if it is a significant blockage, a drop the area of fire sensed by one camera relative to its own history and relative to the other cameras on the scene will be detected. If the duration of the drop is on a time scale faster than the fire at sea can naturally fluctuate, the drop could be flagged. In this case, it does not hurt to drop the blocked area out of the non-burning area summation until the anomaly disappears. The dropping of one part of one camera from the computation will likely not have an adverse effect on the final result as other cameras can record the non-burning area.

The technique of measuring each individual camera's fire area detection live, and dynamically phasing cameras in and out based on large quick intensity drops was used at CRREL sometime after the WPI testing and to filter out the possibility of smoke being counted as non-burning area. Another strategy is simply storing flagged images for review later, when small revisions to the oil burn volume could be made based on this review. There are a number of strategies that need to be carefully considered when transitioning these measurements to operational environments.

7.2. Thickness measurements from free swimming ROV platform

To best transition these acoustic measurements to open water environments will require deployments on multiple platforms. To begin this transition, we deployed the acoustic measurements on a commercial VideoRay Scout ROV as shown in Figure 81 at CRREL. We mounted two transducers with a center frequency of 2.25 MHz on each side of the ROV. The ROV was deployed through a hole approximately 15 feet from the burning oil and flown under the ice to the opening as shown in Figure 82. Flying the ROV and ensuring it would not surface during the burn required some practice but was doable even with poor visibility. During the week, we found the ROV could be operated near enough to the surface to ensure quality thickness measurements without surfacing in the fire.

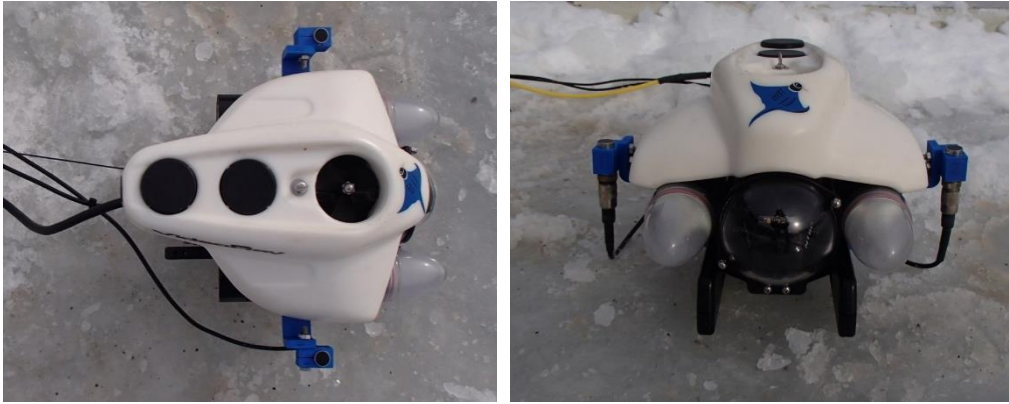


Figure 81. The ROV with two 2.25 MHz transducers mounted on the sides.



Figure 82. The ROV in the water (left) and the oil residue left after burning ANS in the ice field (right).

Figure 83 shows the preliminary measurements of slick thickness measured from the transducers installed on the static frame under the oil and the free-swimming ROV. The resultant slick thickness from both platforms are remarkable similar over the burning period. The slight shift to the left of the ROV thickness measurement was likely caused by the fire moving across the free area seen by the ROV before reaching the fixed frame. Although we believe local thickness variations are small over the oil surface, heavy oil consumption due to burning on one half of the fire will lower thickness which takes time to propagate across the fire. For this project, we did not attempt to measure the spatial variations of the slick thickness.

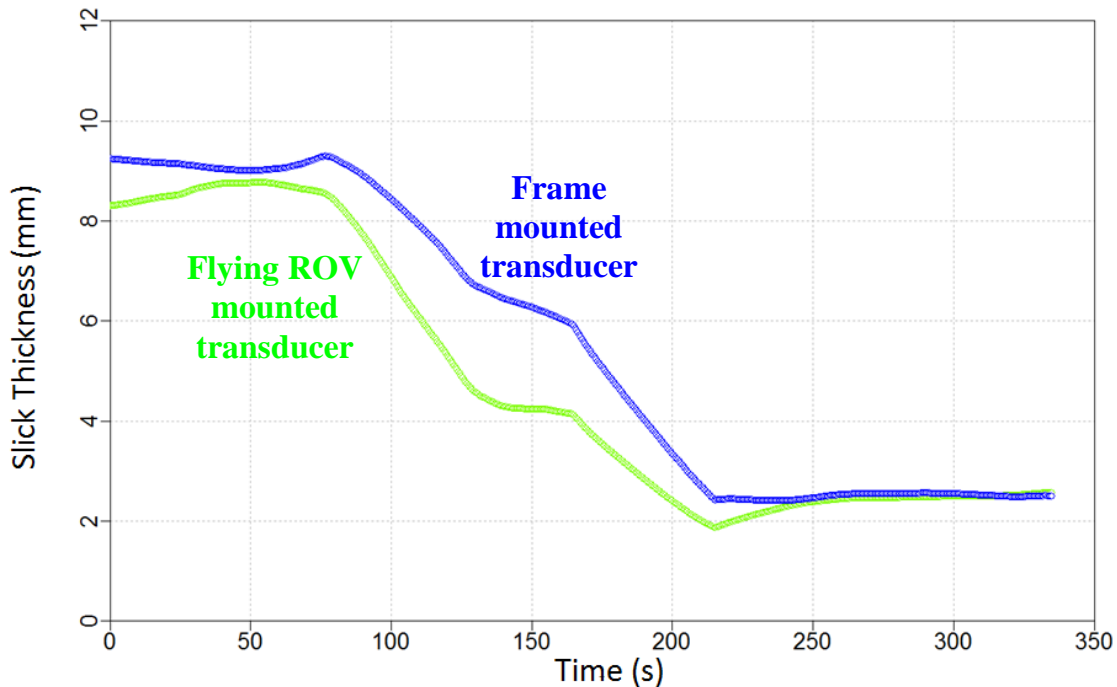


Figure 83. The slick thickness measured by transducers mounted on the frame (blue line) and on the flying ROV (green line) for burn 7.

In open water deployments, the waves and currents will be a challenge that was not experienced in this deployment at CRREL. As part of a separate project, we deployed the acoustic slick thickness measurements on ROV and autonomous underwater vehicle (AUV) platforms and have achieved accurate measurements of the slick thickness in various sea states ranging from harbor chop to ~23 inches in height [5]. In addition to waves and currents it is expected that the oil will weather over time and experience changes in the burning properties due to evaporative losses, photochemical oxidation, and emulsification. Performing these newly development measurements on ISB of weathered oil will be an important part of future work with the measurements on emulsified oils likely being the most challenging because the presence of water in the oil dramatically increases the viscosity and physical properties that affect sound propagation. In addition, the water in the emulsion will likely boil much sooner than the water under the oil which may cause significant fluctuation in the surface of the oil. Studying the acoustic properties of emulsified oil will be important for utilizing these measurements in the field.

8. Summary and Conclusions

We created the capability to measure the instantaneous burn rate and efficiency during ISB to provide a more accurate input into the oil budget and to provide actionable information during ISB operations. The capability is based on surface area measurements

using both visible and IR cameras at various locations around the burning oil and thickness measurements of the slick using acoustic sensors placed in the water under the burning oil. The volume measurements of the oil were benchmarked by weighing the oil during ISB by placing the entire apparatus on a scale and recording the weight during the burn. Our measurements yielded burn rates in the range of 0.6 mm/minute to over 5 mm/minute and efficiencies between 47% and 87% for ANS crude oil in ice fields and controlled indoor fires respectively. The capability developed by this work provides an unprecedented ability to study the dynamics of ISB with sub second time resolution and the potential to measure these parameters in the field when coupled with ROV.

We applied these measurements to ISB of various crude oils at our laboratory, at the burn laboratory at WPI, and in simulated ice fields at the CRREL. We also directly measured the effects of the applications of herders on the thickness and burn rate of oil for applications towards the end of burning, as part of a scoping study. The acoustic thickness measurements were corrected for the high temperature gradient in the oil using a harmonic mean of the speed of sound combined with multi-camera automated burn area estimates to yield an accurate volume of oil consumed while burning. We are able to identify the buildup of the burn, the active burning phase, and in the case of confined burns, the vigorous burning phase where the underlying water boiled. During applications of herders, we were able to measure the thickness increase and surface area contraction and, thus, the increase in combusted oil. The measurements were applied to burning ANS, Rock, Agbami, diesel, and hexane. We also deployed the acoustic measurements of thickness from an ROV platform at CRREL to begin the transition to open water environments.

During this work, we advanced this technology through a tremendous number of Technology Readiness Levels (TRLs). Specifically, at the start of this project the ability to directly measure the volume of burning did not exist. Acoustic measurements of slick thickness had only been used to measure the thickness of non-burning slicks from static platforms or one that rolled along the bottom of the Ohmsett tank, and only the image processing had been attempted on burning oil. At that stage, the technology was at TRL 2. By the end of the project, we advanced the technology through TRL 5 by performing the integrated measurements in the relevant environment at CRREL and started working on TRL 6 by deploying the acoustic measurements from a free swimming ROV platform and image capture from a flying drone platform.

9. Recommendations

Continued advancement of the ISB measurement capability developed in this project should involve three parallel paths. One is to develop a deployable system to measure open water burns. The second is to develop a laboratory measurement apparatus and procedure for determining burn rates and efficiencies of oils. The third path is to determine the effects of oil chemical properties on burn rate and efficiency. Additionally,

it would be useful to use our system to measure the potential improvement of efficiency that could be achieved by the application of herders at various times during burning.

For the field deployable system it will be important to measure the burn area and thickness and archive the results and the supporting imagery to a database for support in post analysis and determination of the volume of oil removed from the environment. The system should allow traversing the burn area with an ROV mounted thickness probe to map the wider oil distribution for accurate volume measurements as well as to guide where to place the boom and boat speeds to optimize the burn rate and efficiency.

Creating a laboratory system for ISB rate and efficiency using the capability developed in this work will be useful for the community because it will provide a turnkey system for determining the burn rates and efficiency of various oils as a function of emulsification, evaporation and photo-oxidation. The scale and shape of the apparatus, the use of water circulation to simulate open water convection, and the amount of oil used to start the burn are all significant in determining burn rates and efficiencies that are transferable to open water burning.

The effects of chemical properties of the oil on the burn rate and efficiency can also be closely studied using the capability developed. It would be important to measure the chemical properties of the oil during the burning by collecting samples throughout the burning process for offline chemical analysis such as the percentage of the sulfur, asphaltenes, resins, and aromatics (SARA) components, density, and spectral analysis. These studies would allow one to determine when each components burns off and how they affect the burn rate and efficiency. In principle, one could perform the chemical analysis on unburned oil and predict the burn rate and efficiency.

10. References

1. Fingas, M. (2016). Controlled in-situ burning of spilled oil, Good practice guidelines for incident management and emergency response personnel. International Association of Oil & Gas Producers.
2. Buist, I., Coe, T., Jensen, D., Potter, S., & Anderson, E. (2003). Oil Spill Response Offshore, In-Situ Burn Operations Manual (No. CG-D-06-03). Coast Guard Research and Development Center, Groton, CT.
3. Panetta, P. D., Byrne, R., & Du, H. (2017, May). The Direct Quantitative Measurement of In-Situ Burn (ISB) Rate and Efficiency. In International Oil Spill Conference Proceedings (Vol. 2017, No. 1, pp. 1006-1019). International Oil Spill Conference.
4. Maul, George A., and James C. Bishop. "Mean Sounding Velocity—A Brief Review." *The International Hydrographic Review* 47.2 (2015).
5. Panetta, Argo, Du, Gong, Ferris, Kidwell, "Development of acoustic methods to measure oil droplet size and slick thickness on ROV and AUV platforms", Report to the Bureau of Safety and Environmental Enforcement, 2017
6. Calvet, L., Gurdjos, P., Griwodz, C, and Gasparini, S, Detection and Accurate Localization of Circular Fiducials under Highly Challenging Conditions, IEEE Conference on Computer Vision and Pattern Recognition, 2016.